POLITECNICO DI TORINO

Dipartimento di Ingegneria Meccanica e Aerospaziale

Corso di Laurea Magistrale in Ingegneria Aerospaziale

Tesi di Laurea Magistrale

Numerical Simulation of a Supersonic Inlet under Off-Design Operating Conditions

Relatori:

Prof. Francesco Larocca

Prof. Andrea Ferrero

Candidato:

Giuseppe Colella

Anno Accademico 2020/2021

A zio Bruno

Abstract

The flow field in an experimentally tested supersonic inlet operating at off-design conditions was investigated numerically, with particular attention to the near-critical and subcritical regimes. Simulations were performed exploiting a research CFD code based on an unstructured finite volumes discretisation scheme and on the Unsteady-RANS equations approach. The Spalart-Allmaras turbulence model was used for closure. The computed results were validated against the experimental findings and compared with other numerical solutions available in the literature.

Keywords: CFD; validation process; finite volumes method; RANS equations; Spalart-Allmaras; supersonic inlet.

Index

List of Figures

List of Tables

1. Introduction

Computational Fluid Dynamics (*CFD*) is the branch of fluid dynamics that aims to solve the governing equations which describe the behaviour of fluids by means of numerical methodologies, exploiting high-performance computers. It represents an extremely powerful tool, capable of providing accurate and reliable descriptions of numerous physical phenomena, as well as dealing with complex geometrical configurations: for these reasons, CFD is nowadays employed in a large variety of research fields, such as aircraft aerodynamics, marine engineering, turbomachinery and meteorology. It constitutes a valid alternative to experimental studies: indeed, numerical simulations allow to analyse systems where experiments are difficult or even impossible to perform, also offering exceptionally detailed results. Furthermore, computational approaches are often more economical than experimental-based techniques, in terms of both time and costs, thus being particularly advantageous in many practical applications.

However, before being available for use, CFD solvers must undergo a *validation process*: considering a particular test case, the computed results must be compared to those of one or more experiments performed on the same problem in order to determine the validity and accuracy of the obtained solution. This process is of fundamental importance, since the implementation of numerical strategies for the resolution of the governing equations inevitably introduces approximation errors that may lead to unreliable results if several possible computational issues are not properly tackled.

The aim of the present work is to conduct a numerical analysis of a supersonic air flow entering the axisymmetric external compression inlet model from Nagashima et al.'s experimental work [1] operating at near-critical and subcritical conditions, with the purpose of validating a research CFD code. Particular attention will be given to *buzz*, an oscillatory phenomenon which represents a serious danger to the engine.

The dissertation is organised as follows: in Chapter 2, several fundamental concepts regarding the aerodynamics of supersonic inlets are presented, and the buzz phenomenon is described in detail; in Chapter 3, the numerical schemes by which the governing equations of fluid dynamics have been discretised are discussed together with grid generation, initial and boundary conditions determination and turbulence modelling; the principal results of the CFD simulations are thoroughly examined and compared with the experimental findings as well as with other computational solutions in Chapter 4; lastly, conclusions and future perspectives are presented in Chapter 5.

2. Supersonic inlets

Inlet aerodynamics has been studied with growing interest since World War II. Several authors have since then attempted to write comprehensive textbooks on this complex subject, and the reader is referred in particular to the works by Seddon et al. [2] and Mattingly et al. [3] for a detailed treatment of the numerous aspects concerning the design of an inlet from both a theoretical and practical perspective.

In this research, we will focus on only one specific category of inlets, that is supersonic inlets, which are intended to operate within a wide range of flight conditions characterised by free-stream Mach number values greater than 1. In the following, we will first recall the definitions of the fundamental parameters by which the performance of an inlet is assessed; then, several basic concepts regarding the different types of supersonic inlets will be presented, and the physical phenomena that occur under various operating scenarios will be described.

2.1. Performance parameters

The performance of a supersonic inlet is determined by three main parameters: total pressure ratio (η_d), mass-flow - or capture-area - ratio (ϕ_d) and inlet drag (D). The overall efficiency and usefulness of any inlet must be evaluated by considering all these characteristics simultaneously, as the improvement in one of them is often obtained at the expense of the others: compromises are therefore needed in the design process. Furthermore, rapid deterioration of these parameters during off-design operations must be avoided in order to preserve engine function under varying flight conditions.

i. Total pressure ratio

The total pressure ratio is defined as:

$$\eta_d = \frac{p^0_{exit}}{p^0_0} \quad (2.1)$$

where p^0_{exit} is the total pressure at the exit of the inlet and $p_0{}^0$ is the free-stream total pressure. It is influenced by the shock and viscous losses generated by the interaction between the flow and the inlet's walls, and its values are always lower than 1.

ii. Mass-flow ratio

The mass-flow ratio is defined as:

$$\phi_d = \frac{\dot{m}}{\dot{m}_{id}} \quad (2.2)$$

where $\dot{m}$ is the mass-flow rate that effectively enters the inlet and $\dot{m}_{id}$ is the maximum mass-flow rate that could enter the inlet. As represented in Figure 2.1, $\dot{m}$ can also be seen as the mass-flow rate associated with the entering stream tube of cross-sectional area A_0, whereas $\dot{m}_{id}$ can be defined as the mass-flow rate associated with the cross-sectional area A_i of the inlet's entrance.

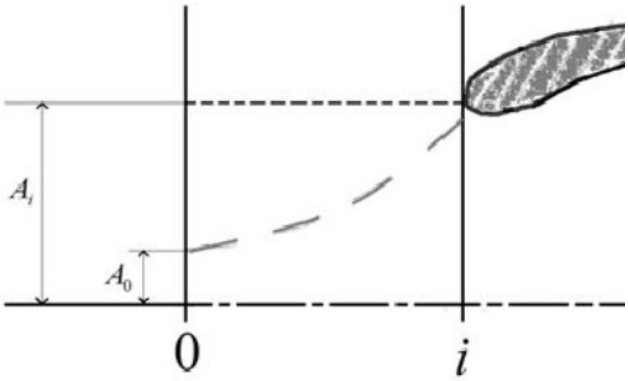

Figure 2.1. Comparison between the cross-sectional area of the entering stream tube and the cross-sectional area of the inlet's entrance

The mass-flow ratio can therefore be re-written as a capture-area ratio, using the continuity equation:

$$\phi_d = \frac{\dot{m}}{\dot{m}_{id}} = \frac{\rho_0 V_0 A_0}{\rho_0 V_o A_i} = \frac{A_0}{A_i} \quad (2.3)$$

The condition:

$$\phi_d = 1 \quad (2.4)$$

implies that there is no flow spillage, i.e. that the entering stream tube's cross-sectional area is equal to the cross-sectional area of the entrance.

iii. Inlet drag

The total drag of the inlet can be defined as the sum of several components, namely the wave drag (D_w), the skin friction drag (D_f) and the additive drag (D_a):

$$D = D_w + D_f + D_a \quad (2.5)$$

The first two contributions are sometimes identified as cowl drag, since it is the interaction between the flow and the cowl that gives rise to shock waves and boundary layers.

The third component, on the other hand, is directly linked to spillage and accounts for a large part of the total inlet drag when external strong shocks are present. Additive drag is defined as the difference between the stream force at the inlet's entrance and the stream force associated with the free-stream flow, and is often expressed in its non-dimensional form:

$$\widetilde{D}_a \triangleq \frac{D_a}{p_0 A_i} = \frac{p_i}{p_0}\left(1 + \gamma M_i^2\right) - 1 - \phi_d \gamma M_0^2 \quad (2.6)$$

where A_i is the cross-sectional area of the inlet's entrance, p_0 is the free-stream static pressure, p_i is the static pressure at the inlet's entrance, M_0 is the free-stream Mach number, M_i is the Mach number of the flow at the inlet's entrance, ϕ_d is the mass-flow ratio and γ is the ratio of specific heats. It is important to notice that, in the absence of flow spillage, the additive drag is null.
Minimising total drag is one of the principal project requirements.

iv. Other design variables

Alongside these three main characteristics, there are other factors that may have an influence on the inlet's performance.
One of them is flow distortion, which indicates an uneven pressure distribution over the inlet's exit area that produces low burning efficiency, even for high total pressure ratios, and can in some cases lead to engine flameout: determining its magnitude is therefore important, especially for high values of angle of attack.
The presence of control systems, such as boundary layer bleed and bypass, has to be considered as well.
The location of the inlet on the wing or fuselage, the aircraft attitude and possible noise suppression requirements represent further design variables.

2.2. Internal compression inlets

Supersonic inlets are commonly classified into three different types - internal, external and mixed compression - depending on the location of the compression waves system.
Internal compression inlets consist of a simple convergent-divergent duct: the incoming flow is compressed by means of multiple oblique shock waves followed by a normal shock, located in a stable position downstream of the throat during normal operation (Figure 2.2).

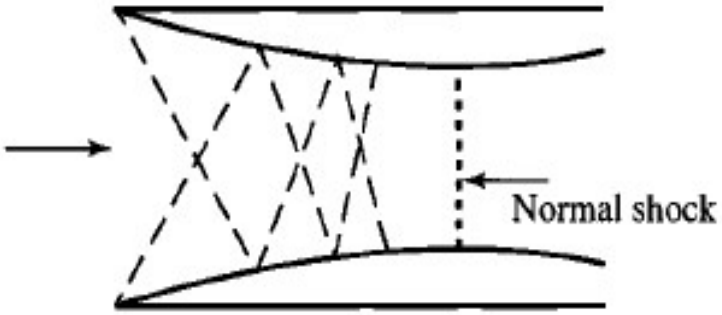

Figure 2.2. Compression waves system for an internal compression inlet during normal operation

Despite its elementary design, the usefulness of this type of supersonic inlet is limited by several problems that arise when it faces off-design operating conditions. When the flight Mach number (*M*) is greater than 1, but less than the normal operation value, a normal shock appears ahead of the cowl lip (Figure 2.3): the inlet is said to be *unstarted*. In this situation, the total pressure ratio and the mass-flow ratio decrease, thus possibly causing engine flameout, while additive drag substantially increases. In order to *start* the inlet, a variation of the throat's cross-sectional area is needed: if this area is made large enough for the normal shock to reach the inlet's entrance, the normal operation conditions can be restored.

The need for large area variations, together with the poor performance at angles of attack, have led to the demise of internal compression inlets, which nowadays are mostly of academic interest.

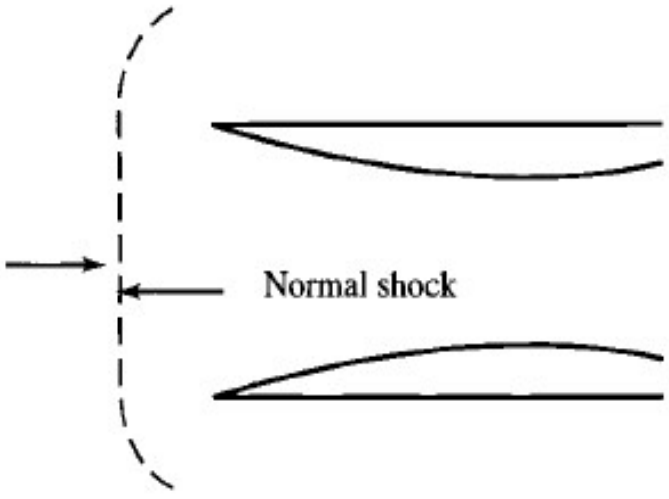

Figure 2.3. Unstarted internal compression inlet

2.3. External compression inlets

External compression inlets achieve compression through either a single normal shock or a series of oblique shocks followed by a normal shock.

Inlets of the first type are called *Pitot inlets* (Figure 2.4), and are simple, short, lightweight and inexpensive. Their total pressure ratio is equal to the value associated with the normal shock, and therefore depends solely on the free-stream Mach number: as M increases, η_d decreases, and for Mach numbers above 1.6 this performance parameter becomes too low, rendering Pitot inlets inefficient.

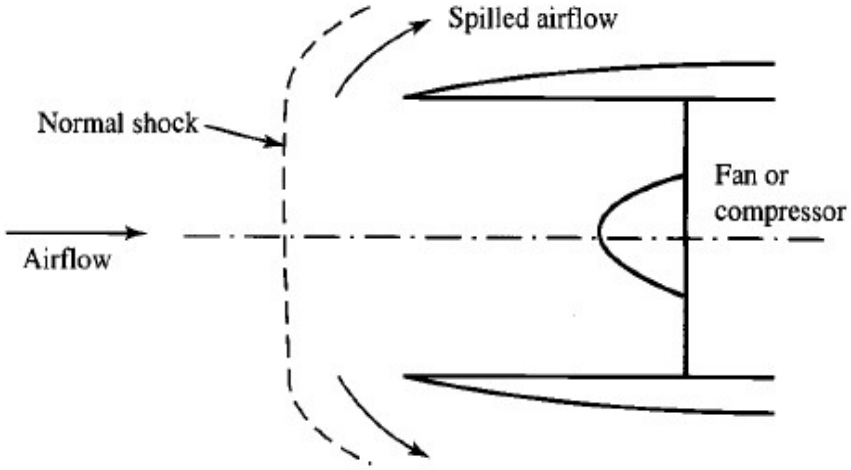

Figure 2.4. Pitot inlet

Inlets of the second type are somewhat more complex: as shown in Figure 2.5, they are composed of a *cowl*, a *center body*, on which one or more ramps are present, and a *diffuser*. The ramps precede the inlet's entrance, which often corresponds to the throat, and generate the oblique shocks. On-design operation is with the normal shock located at or very near the cowl lip: this scenario is also referred to as *critical operation*.

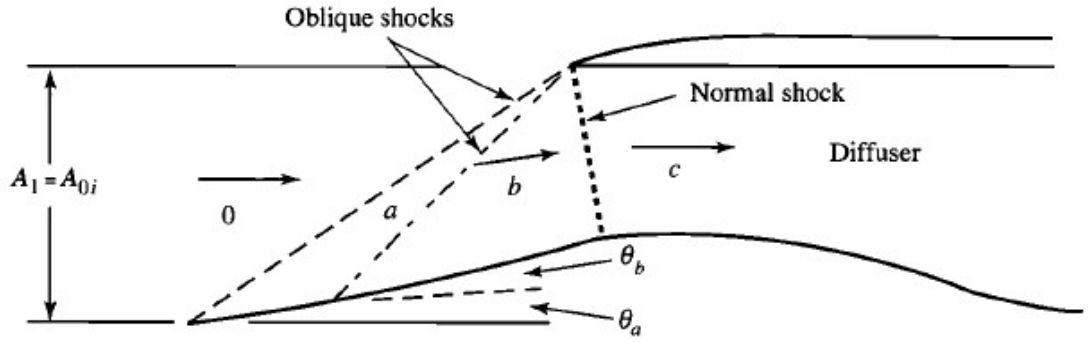

Figure 2.5. External compression inlet at critical operation

By compressing the flow through a series of weak oblique shocks followed by a normal shock instead of exploiting a single normal shock, the total pressure ratio is increased

for the same free-stream Mach number (Figure 2.6). Nevertheless, due to the presence of the ramps, the flow is deviated from the axial direction, which has to be restored by the diffuser: this may lead to additional length, weight and friction and pressure losses.

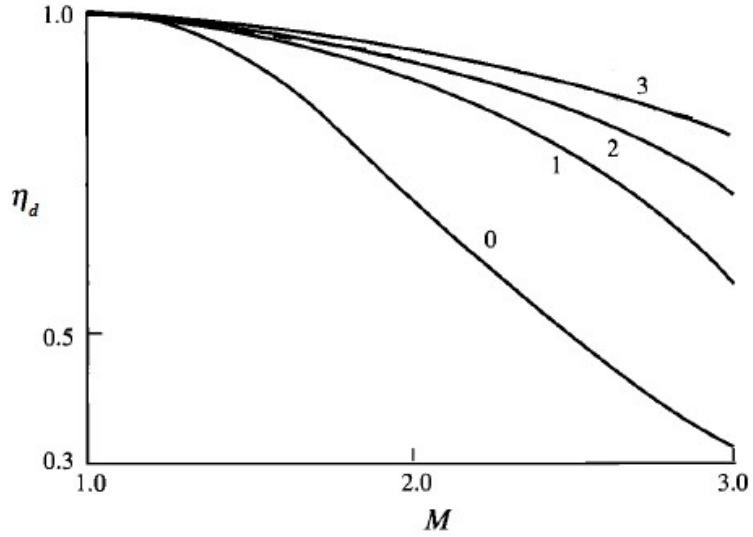

Figure 2.6. Total pressure ratio as a function of free-stream Mach number for an external compression inlet with one or more oblique shocks of the same strength (curve 0 is representative of a Pitot inlet)

The total pressure ratio for the generic external compression inlet of the second type can be evaluated using the well-known relations for normal and oblique shocks. Total pressure variation across a normal shock is calculated as follows:

$$\frac{p_2^0}{p_1^0} = \left[1 + \frac{2\gamma}{\gamma+1}(M_1^2 - 1)\right]^{\frac{1}{\gamma-1}} \cdot \left[\frac{(\gamma+1)M_1^2}{(\gamma-1)M_1^2 + 2}\right]^{\frac{\gamma}{\gamma-1}} \quad (2.7)$$

where p_1^0 is the total pressure upstream of the shock, p_2^0 is the total pressure downstream of the shock, M_1 is the upstream Mach number and γ is the ratio of specific heats. Downstream Mach number (M_2) is determined by the relation:

$$M_2 = \sqrt{\frac{1 + \left(\frac{\gamma-1}{2}\right)M_1^2}{\gamma M_1^2 - \frac{\gamma-1}{2}}} \quad (2.8)$$

Expressions (2.7) and (2.8) are formally identical for the case of an oblique shock, but upstream and downstream Mach numbers have to be substituted by *normal* Mach numbers, defined as:

$$M_{1n} = M_1 \sin(\beta) \quad (2.9a)$$

$$M_{2n} = M_2 \sin(\beta - \vartheta) \quad (2.9b)$$

where β is the angle of deflection of the shock with respect to the upstream flow direction and ϑ is the ramp angle (Figure 2.7).

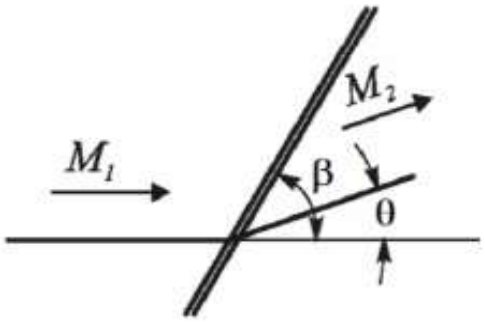

Figure 2.7. Generic oblique shock configuration

Upstream Mach number (M_1), β and ϑ are linked together by the so-called *theta-beta-Mach relation*:

$$\tan(\vartheta) = \frac{2}{\tan(\beta)}\left[\frac{M_1^2(\sin(\beta))^2 - 1}{M_1^2(\gamma + \cos(2\beta)) + 2}\right] \quad (2.10)$$

which is usually plotted as a diagram (Figure 2.8):

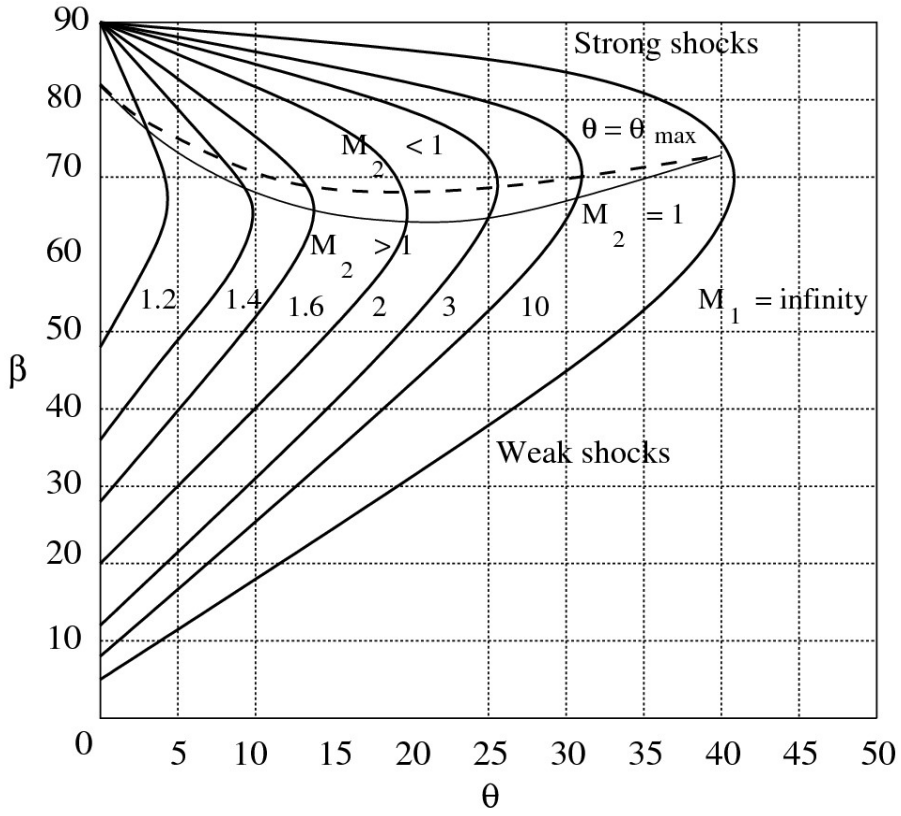

Figure 2.8. ϑ-β-M diagram [4]

It can be seen from Figure 2.8 that, for a fixed upstream Mach number value, the theta-beta-Mach function has two zeros:

$$\vartheta = 0 \rightarrow \beta = \frac{\pi}{2} \quad (2.11a)$$

$$\vartheta = 0 \rightarrow \beta = \arcsin\left(\frac{1}{M_1}\right) \quad (2.11b)$$

The first zero corresponds to the case of a normal shock, while the second zero indicates an isentropic compression (*Mach wave*). It must be also noticed that this function has a maximum value (ϑ_{max}) that changes with the upstream Mach number: this implies that, at a given M_1, oblique shock solutions exist for a certain range of ramp angles only, whereas for ϑ greater than ϑ_{max} only detached shocks can be created.
The total pressure ratio of the inlet is finally calculated as the product of the total pressure variations across the different shocks:

$$\eta_{d,tot} = \prod_i \eta_{d,i} \quad (2.12)$$

As explained before, critical operation of the inlet is achieved when the normal shock is located at or very near the cowl lip (Figure 2.5): in this situation, the mass-flow ratio reaches its peak, and the inlet is *matched* to the engine. However, it must be observed that, in the majority of cases, inlets are designed in order for the oblique shocks not to touch the cowl lip at critical conditions, with the aim of avoiding shock-boundary layer interactions: consequently, flow spillage is not null, as shown in Figure 2.9.

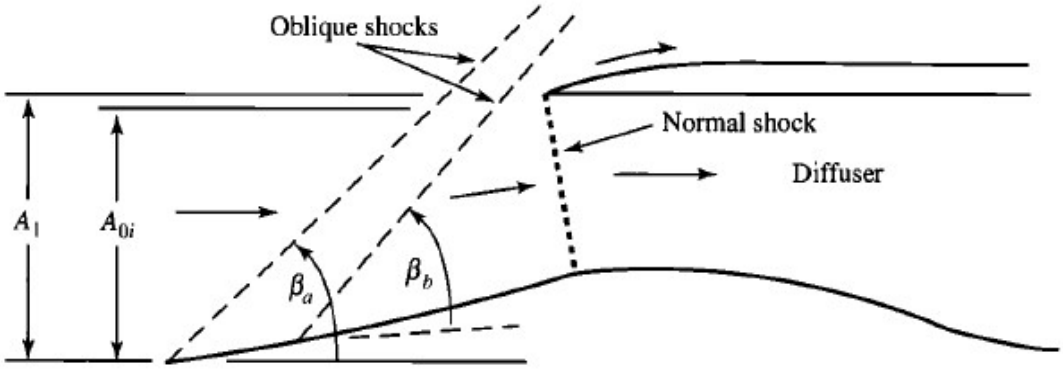

Figure 2.9. External compression inlet at critical operation with flow spillage

At a given flight Mach number, changes in engine throttle lead to off-design operating conditions. Engine throttle variations correspond to variations in the *corrected* mass-flow rate, which is a function of the inlet's exit Mach number (M_{exit}): the engine is

requiring a smaller or greater amount of air, hence the inlet has to adapt to the new situation.

When the corrected mass-flow rate decreases below its critical value ($M_{exit}<M_{exit,cr}$), the inlet is said to be operating at *subcritical* conditions (Figure 2.10): the normal shock is forced to move upstream of the throat, thus increasing flow spillage - and, therefore, additive drag - whilst diminishing the mass-flow ratio.

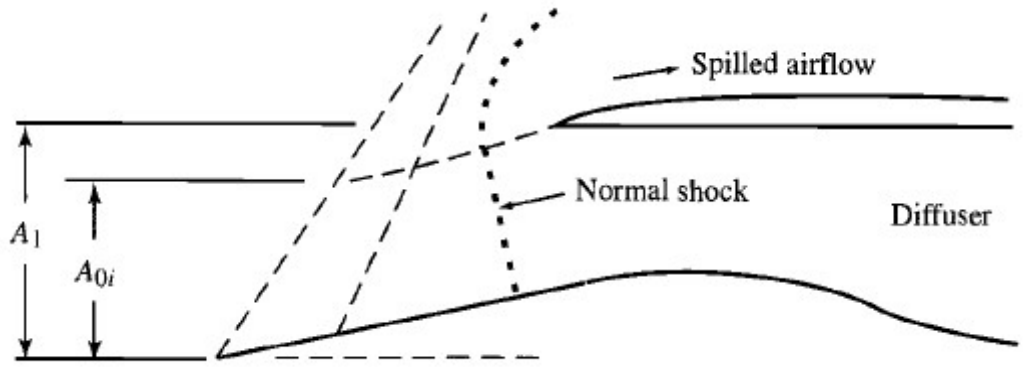

Figure 2.10. External compression inlet at subcritical operation

When, on the other hand, the exit Mach number increases above its critical value ($M_{exit}>M_{exit,cr}$), the inlet is not capable of capturing the required mass-flow rate and the normal shock moves downstream of the throat: this scenario is defined as *supercritical* operation (Figure 2.11). Supercritical operation causes the total pressure ratio to drop significantly, since the shock's strength increases as it moves into the diffuser: for this reason, this particular regime has to be avoided if possible.

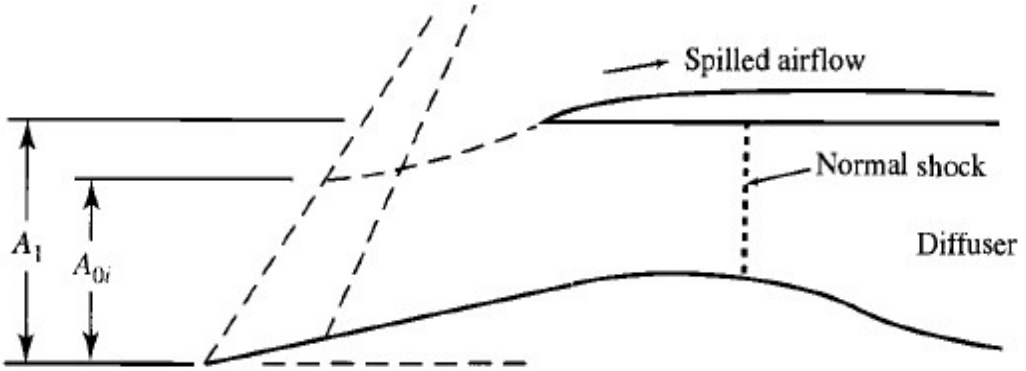

Figure 2.11. External compression inlet at supercritical operation

The external compression inlet's performance at various operating conditions is typically plotted as a map, whose *x* and *y* axes represent the mass-flow ratio and the total pressure ratio respectively (Figure 2.12). Here, it can be noticed that during subcritical operation the inlet reaches a stability limit, identified by a minimum allowable

value of the mass-flow ratio: this feature represents the subject matter of a following section in this chapter.

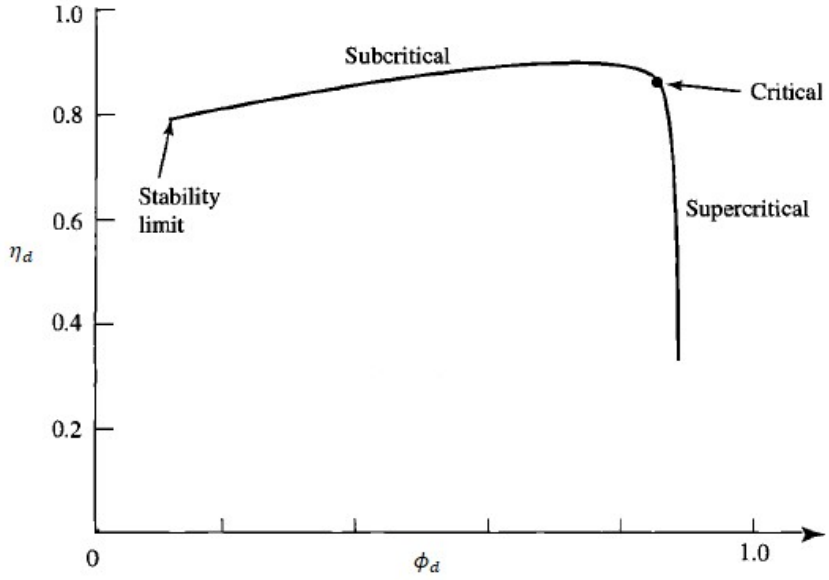

Figure 2.12. Typical external compression inlet's performance map

If the free-stream Mach number changes during flight, the strength of the shock system and the inclination of the oblique shocks with respect to the axial direction are modified, thus varying both the total pressure and mass-flow ratio. Consequently, the curve in Figure 2.12 is translated. When in particular the free-stream Mach number is increased, the total pressure ratio diminishes, whilst the mass-flow ratio augments. Cowl drag is increased as well in this situation, and the performance of the external compression inlet of the second type becomes unacceptable for flight Mach numbers above 2.5. Moreover, since the characteristics of the entering flow vary with both engine throttle settings and free-stream Mach number, variable geometry inlets are sometimes needed in order to enhance the performance, and a higher degree of design complexity is therefore required.

2.4. Mixed compression inlets

At flight Mach numbers greater than 2.5, satisfactory performance is obtained by using mixed compression inlets. These inlets, as the name implies, achieve compression through external and internal oblique shocks followed by a terminal normal shock, located downstream of the throat during normal operation (Figure 2.13). The mixed compression inlet can be seen a fusion of the internal and external types, and is therefore more complex, heavier and more expensive. Similar to the internal compression inlet, the mixed compression inlet also requires a variable cross-sectional

area at the throat, although this variation is smaller in comparison to the purely internal compression case.

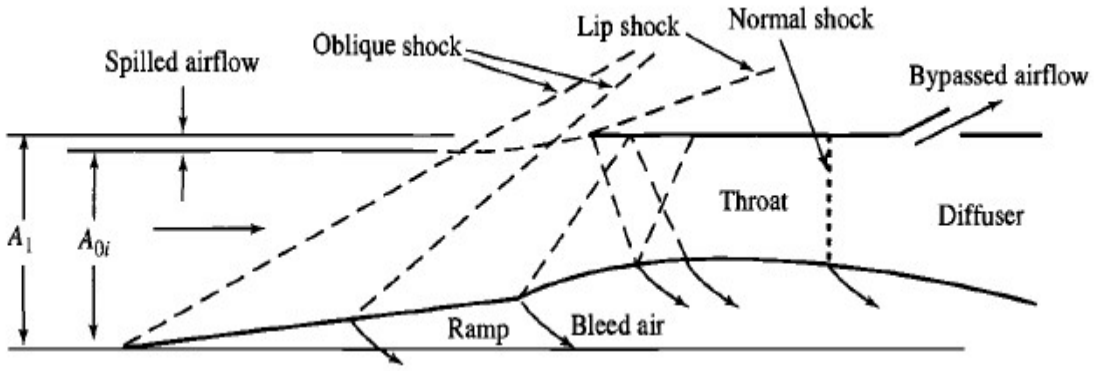

Figure 2.13. Mixed compression inlet during normal operation

2.5. Two-dimensional and axisymmetric supersonic inlets

Supersonic inlets can furthermore be classified as two-dimensional and axisymmetric (Figure 2.14). The former are simpler to design and are capable of providing a larger variation in the entering flow, whilst the latter are lighter and allow to obtain higher total pressure ratios for the same flight Mach number. Axisymmetric inlets, however, pose the problem of effectively implementing boundary layer bleed systems on the center body through the support struts.

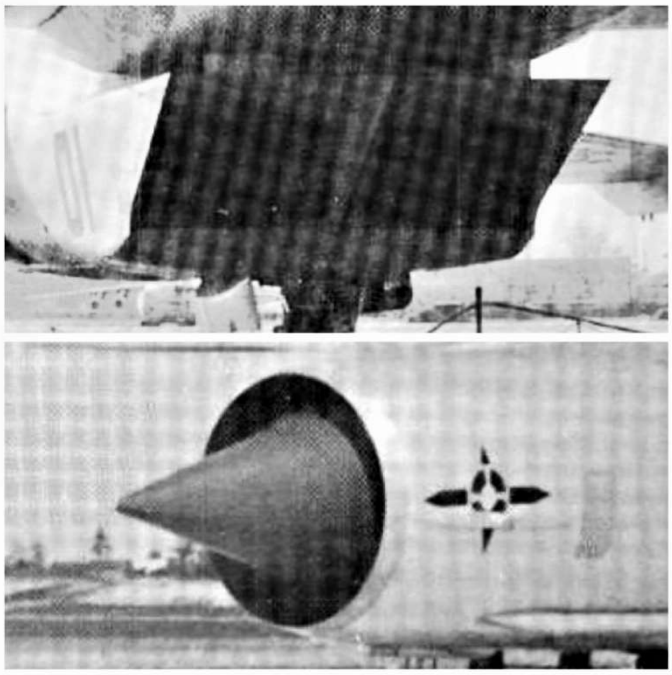

Figure 2.14. Two-dimensional (top) and axisymmetric (bottom) supersonic inlets [5]

2.6. Buzz

In Section 2.3, it has been observed that external compression inlets operating in the subcritical regime may reach a stability limit (Figure 2.12), i.e. a minimum mass-flow ratio value for which the entering flow is stable. Below this point, a new, non-stationary phenomenon occurs: *buzz*. It is characterised by high frequency and/or high amplitude shock oscillations about the inlet's entrance, which cause large variations in the mass-flow and pressure ratios over a short period of time, thus leading to thrust loss, inefficient combustion or flameout and, in extreme cases, structural damages to the engine.

2.6.1. Buzz onset

Buzz was first observed by Oswatitsch in 1944 [6] and has been largely investigated since, both experimentally and numerically. It is nowadays well established that this phenomenon is triggered by either a vortex sheet, generated from the intersection of normal and oblique shocks and moving across the cowl lip (*Ferri criterion*), or a shock-induced separation, that develops on the compression surface and obstructs the inlet's entrance (*Dailey criterion*).

The Ferri criterion was introduced by Ferri and Nucci in 1951 [7]. They observed that shock oscillations are initiated when the vortex sheet generated from the intersection of normal and oblique shocks impinges on the cowl lip and moves from the outside to the inside (Figure 2.15): as soon as the vortex sheet has entered the inlet, boundary layer separation occurs on the cowl's inner surface, thus increasing flow spillage and pushing the normal shock upstream. This, in turn, causes the vortex sheet to move away from the cowl, allowing the flow to reattach and the shock to travel downstream to its initial position. However, this implies that the vortex sheet also returns to its previous position, and separation is generated once again. Such oscillation cycle is sometimes referred to as *little* or *low buzz*.

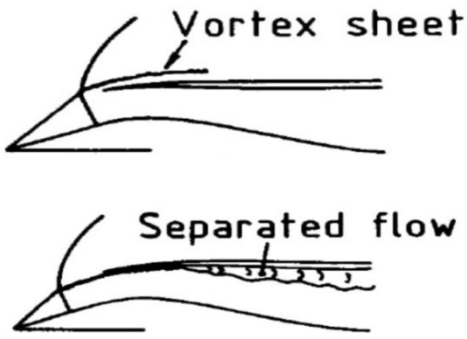

Figure 2.15. Vortex sheet moving across the cowl lip, from the outside (top) to the inside (bottom)

The Dailey criterion owes its name to Charles L. Dailey, who studied the buzz phenomenon for his PhD dissertation in 1954 [8]. He noticed that buzz begins when boundary layer separation occurs at the shock foot, due to the adverse pressure gradient generated across the discontinuity: this separated flow area gradually grows and obstructs part of the inlet's entrance, forcing the shock to move upstream towards the tip of the center body (*subcritical phase*). Then, the shock system oscillates at a high frequency around the tip (*secondary oscillations*), before moving rapidly back into the inlet, thus choking it (*supercritical phase*). Dailey explained that, during the high frequency oscillations phase, the inlet's entrance is almost completely blocked: this situation causes the internal pressure to decrease to a point that eventually allows the shock to move downstream again. Finally, throughout the supercritical phase, there is a gradual refilling of the inlet that pushes the shock upstream to its initial position, and a new cycle starts. This kind of buzz is sometimes referred to as *big* or *high buzz*. Figure 2.16 shows a complete big buzz cycle on an *isentropic spike*, which is a particular type of external compression inlet.

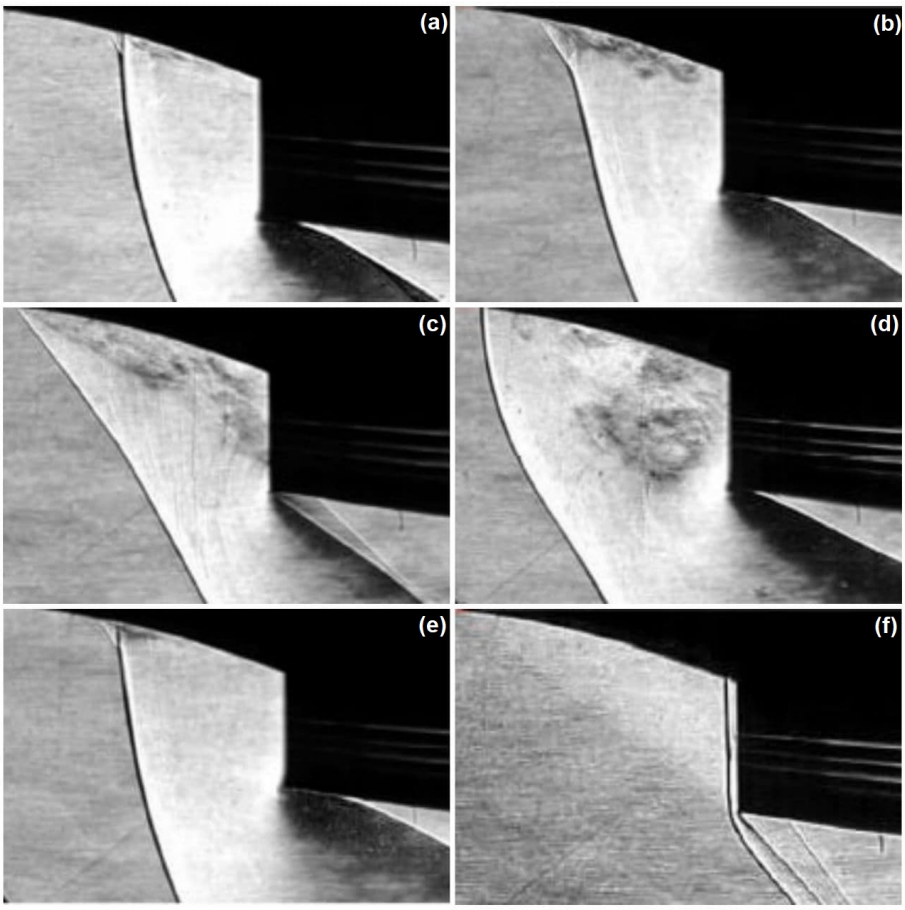

Figure 2.16. Schlieren images of a Dailey type buzz cycle, representing its three main phases: subcritical (a-b), secondary oscillations (c-e), supercritical (f) [9]

2.6.2. Studies on buzz

Many researchers have focused their attention on buzz, since a thorough understanding of the phenomenon is fundamental to predicting and avoiding its onset or, possibly, tackle its detrimental effects. There is, therefore, a large number of experimental and numerical works on this subject.

In 1972, Nagashima et al. [1] conducted an experiment on an axisymmetric external compression inlet, whose center body could be translated along the axial direction, to study the characteristics of buzz for different geometrical configurations and angles of attack. Starting from supercritical conditions and gradually reducing throttle, they discovered that the non-stationary phenomena occurring below the stability limit were characterised by different frequencies, depending on the throttle ratio value: low buzz was observed for relatively high throttle ratios and presented a dominant frequency around 120Hz, whereas high buzz arose when the throttle was further reduced and presented a dominant frequency around 360Hz. The amplitude of these oscillations was found to vary arbitrarily. Nagashima et al. also proposed a one-dimensional acoustic model, based on the resonance theory, in order to predict buzz characteristic frequencies: by considering the inlet as a circular duct, they obtained such frequencies as the solution of the wave equation for disturbance velocity potential with imposed boundary conditions, namely the presence of a shock wave at the inlet's entrance and a choked rear exit. They nonetheless pointed out that their model was extremely simplified, since it neglected the presence of the center body, and completely inadequate to explain the instability of the system.

Hankey and Shang [10] dilated upon the physical origin of buzz from an aeroacustics perspective and improved Nagashima's model introducing the concept of self-excited oscillations, defined as motions in which the sustaining force is created by the motion itself. They observed that separated flows possess a relatively low natural frequency, for which they are likely to be self-sustained if a positive *feedback mechanism* from the acoustical field to the source is present. This feedback, consisting of standing pressure waves reflected by the exit throat and travelling upstream through the subsonic separated shear layer, is enhanced by the accumulation of acoustical energy in the resonator, represented by the inlet. However, such mechanism is non-linear, so it cannot be predicted using linear theories: for this reason, Hankey and Shang stated that Nagashima's model, which was based on the linearised potential equation, was "doomed to failure", and that the rotational equations should be considered instead. They therefore calculated the characteristic frequencies of a self-sustained oscillation using the modified Rossiter equation [11]:

$$f_m = \frac{mU_e}{L(M_0 + k^{-1})} \quad m = 1,2,3 \ldots \quad (2.13)$$

where m is the mode number, U_e is the kinematic velocity, L is the length of the resonator, which separates the acoustic source from the reflection surface, M_0 is the Mach number, defined as:

$$M_0 = \frac{U_e}{a_0}$$

where a_0 is the speed of sound, and k is a nondimensional parameter, defined as:

$$k = \frac{c_r}{U_e}$$

where c_r is the speed of the pressure waves travelling downstream, i.e. before being reflected. Hankey and Shang concluded that if one of the resulting frequencies is sufficiently close to the natural frequency of the separated flow, then positive feedback is obtained (*overblowing*) and self-excited oscillations are initiated.

Newsome [12] performed the first computational study on buzz in 1984. He chose Nagashima's axisymmetric inlet as the experimental model for comparison, and implemented the MacCormack's explicit finite differences scheme for the numerical integration of the Reynolds-Averaged Navier-Stokes (RANS) equations combined with the Cebeci-Smith algebraic model for the turbulent eddy viscosity. His results agreed well with the available data and several features of the buzz instability were satisfactorily represented by the numerical solution.

Lu et al. [13] adopted Dailey's ramjet engine as the model for their numerical simulations of buzz, in which they used a high-resolution total variation diminishing (TVD) scheme. Lu et al. also proposed another correction to Nagashima's acoustic model, underlining the fact that the inflow boundary condition should be modified according to the phase of the buzz cycle, and that the characteristic frequencies of the oscillations are therefore dependent on the upstream flow. They furthermore provided a detailed explanation of the feedback mechanism introduced by Hankey et al. for the subcritical and supercritical phases of the cycle separately, partly correcting the American researchers. They observed that during the subcritical phase feedback is generated from the vortexes that impinge on the cowl lip and the center body and create pressure waves that travel upstream and push the shocks system towards the tip, whereas during the supercritical phase feedback is given by the plenum chamber, since the normal shock is positioned into the inlet and the vortexes at the cowl lip no longer exist. The source of acoustic signals throughout the supercritical phase is

represented by the separated area generated downstream of the internal shock: these signals resonate with the characteristic frequencies of the plenum chamber and produce an expulsive pressure that forces the shock to move back upstream. Lu's explanation of the buzz cycle thus backed Dailey's initial hypotheses, whilst offering further insights on the acoustic mechanisms that underlie such non-stationary phenomenon.

Trapier et al. studied buzz in a rectangular mixed compression inlet, first experimentally [14] and then also numerically [15], for different free-stream Mach numbers. Three-dimensional Delayed Detached-Eddy Simulations (DDES) were conducted, in order to combine the best features of RANS and Large Eddy Simulations (LES) approaches. Both little and big buzz were observed, but, contrarily to the findings of Nagashima et al., they were characterised by small amplitudes and high dominant frequencies and great amplitudes and low dominant frequencies respectively: these somewhat contradictory results highlight the strong dependence of the phenomenon's features on the geometrical configuration. Trapier et al. furthermore studied the effect of boundary layer bleed on flow instability, and showed that buzz limit was shifted to a lower mass-flow ratio value for the lowest free-stream Mach number. Bleed devices also brought considerable improvements in terms of pressure recovery, but at the expense of the captured mass flow, which was reduced.

An axisymmetric low-boom supersonic inlet was analysed numerically by Chima in 2012 [9], exploiting data from previous wind tunnel tests. Central difference Rusanov scheme was combined with Van Leer upwind scheme for unsteady simulations in order to avoid non-physical spatial oscillations. Although the results agreed well with Dailey's description of the buzz cycle, Chima's analysis did not back up Hankey's acoustic wave model, as the modified Rossiter equation (2.13) predicted a frequency almost twice the computed one. This was explained by observing that the primary shock system, located on the isentropic spike, did not reflect the upstream-running waves, and that standing waves could therefore not be supported. Chima furthermore found that, throughout the secondary oscillations phase of the buzz cycle, fairly strong normal shock waves were generated at the tip and moved downstream through the inlet, before being partially reflected at its exit, thus creating a system of shocks travelling in both directions.

In his dissertation, Hong [16] numerically investigated buzz under different throttling and angle of attack conditions, using Nagashima's configuration. He attempted to find a connection between buzz transitional phases - from low to high buzz and vice versa - that occur when throttle is varied and the acoustic phenomenon of overblowing, by observing that decreasing throttle ratios behave analogously to increasing jet velocities

in wind instruments, and that the vortexes impinging on the cowl and the center body play the role of the *edge tones*, whilst the diffuser acts as a resonator. Hong noticed that a decrease in throttle ratio leads to a greater flow instability, thus giving rise to new vortexes and consequently to new pressure waves: as soon as the interaction between such waves and the resonator returns a positive feedback, the switch from lower to higher dominant frequencies is obtained. A similar analysis was conducted for increasing throttle ratios, the sole difference being the variation from higher to lower dominant frequencies: a hysteretic behaviour of buzz was therefore suggested. From a numerical perspective, Hong also compared the results obtained by axisymmetric and three-dimensional simulations using the same numerical schemes, and noticed that buzz in the axisymmetric case occurred at a higher throttle ratio than the three-dimensional computation. He explained this difference by stating that axisymmetric simulations do not take three-dimensional flow effects into account, thus causing a slight reduction in the mass-flow ratio: for this reason, axisymmetric simulations were compared - and agreed well - with the experimental results after “shifting” the throttle ratio values.

Luo et al. [17] also studied buzz in Nagashima’s inlet, implementing an Unsteady-RANS approach with the Spalart-Allmaras turbulence model. Their aim was to describe static pressure oscillations analytically by using an innovative and elegant tool, known as *Proper Orthogonal Decomposition* (*POD*) *Method* [18], which allowed them to approximate the complex flow field with its most energetic modes only, namely the first and second-order POD modes, representing the average and fluctuating pressure distributions respectively. The evolution of the second-order mode was in particular identified as the most suitable to describe buzz characteristics: the fluctuating pressure was therefore mathematically modelled as the product of two sinusoidal waves, thus decoupling the spatial and temporal terms. This simplification allowed the authors to find an analytical expression for the pressure field inside the inlet during buzz. Luo et al. furthermore proposed a buzz suppression mechanism, consisting of an intermittent air jet positioned at the inlet’s entrance, characterised by the same frequency of the second-order mode’s oscillations and a phase displacement $\Delta\phi=\pi$. Such mechanism was proved capable of enhancing flow stability and partially controlling buzz, thus widening the engine’s operative range.

3. Numerical methods

Fluid motion is governed by the *conservation laws*, which express the total variation of a certain flow quantity inside an arbitrary volume as the net effect of the transport of such quantity across the volume's boundaries, the action of internal and/or external forces on the volume and the presence of sources inside the volume. These laws form a system of non-linear partial differential equations (PDEs), which cannot be solved exactly, except for a small number of particular cases: it is therefore necessary, for practical applications, to implement *numerical methods* that allow to find approximate solutions by means of iterative processes. The science that utilises such tools to simulate complex fluid flows is known as *computational fluid dynamics* (*CFD*).

In the following, we will first introduce the governing equations of fluid dynamics, formulated as the so-called *Navier-Stokes equations*. Then, we will focus our attention on the spatial and temporal discretisation schemes adopted in the present work, as well as on grid generation and on time step selection. Turbulence and its modelling will also be discussed. Finally, we will dilate upon the determination of initial and boundary conditions for our problem. The reader is referred to the works by Blazek [19] and Versteeg et al. [20] for further understanding of the numerous schemes and models employed in modern CFD solvers.

3.1. Governing equations

As anticipated, the dynamical behaviour of a fluid is determined by three conservation laws, namely the mass (or *continuity*), momentum and energy equations.

i. Continuity equation

Let us consider a finite control volume (Ω), fixed in space, as represented in Figure 3.1:

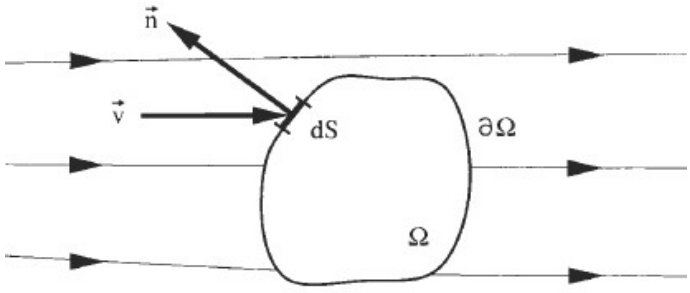

Figure 3.1. Finite control volume (Ω) bounded by a closed surface (∂Ω). Here, dS represents an elemental surface area, and n is the associated unit normal vector

The mass conservation law states that mass variations inside this volume over time are solely due to the mass fluxes across the control surface ($\partial\Omega$).

The time rate of change of the mass inside the volume can be expressed as:

$$\frac{\partial}{\partial t}\int_{\Omega} \rho \, d\Omega$$

where ρ is the fluid density and represents the conserved quantity.
The mass flow through the entire control surface can be written as the sum of the fluxes across each elemental surface area (dS):

$$-\oint_{\partial\Omega} \rho\bar{v} \cdot \bar{n} \, dS$$

where $\bar{v}$ is the velocity vector and $\bar{v} \cdot \bar{n}$ represents the velocity component perpendicular to the surface element. The sign is determined by the convention imposed on the orientation of the unit normal vector ($\bar{n}$), that points out of the control volume.
Since mass cannot be created - nor destroyed - for a single-phase fluid, and therefore no source terms are present, the mass conservation law can finally be written as:

$$\frac{\partial}{\partial t}\int_{\Omega} \rho \, d\Omega + \oint_{\partial\Omega} \rho\bar{v} \cdot \bar{n} \, dS = 0 \quad (3.1)$$

Equation (3.1) represents the continuity equation in its *integral conservative formulation*, which is characterised by the important property of remaining valid in the presence of discontinuities in the flow field, such as shocks. For this reason and for its generality, this formulation is used in the majority of modern CFD codes.

ii. Momentum equation

Let us consider the finite control volume of Figure 3.1 again. The momentum conservation law, that descends from Newton's second law of motion, states that momentum variations inside this volume over time are due to the momentum fluxes across the control surface and to the contribution of several source terms.
The variation with time of momentum within the control volume can be expressed as:

$$\frac{\partial}{\partial t}\int_{\Omega} \rho\bar{v} \, d\Omega$$

Similarly to the case of the continuity equation, the transport of momentum across the control surface is given by:

$$-\oint_{\partial\Omega} (\rho\bar{v})\bar{v}\cdot\bar{n}\,dS$$

The source terms are represented by the external (or *volume*) and internal (or *surface*) forces acting on the control volume. The former are defined as forces that act on the system's mass - e.g. gravitational or electromagnetic forces - and can be written as:

$$\bar{F_v} = \int_{\Omega} \rho\bar{f_e}\,d\Omega$$

where $\bar{f_e}$ is a generic volume force per unit mass. The latter, on the other hand, act directly on the control surface and result from the combination of the pressure distribution imposed by the outside fluid that surrounds the control volume and the shear and normal stresses caused by the friction between the fluid and the control surface. Internal forces can therefore be defined as the sum of two terms:

$$\bar{F_s} = \oint_{\partial\Omega} \left(-p\bar{\bar{I}} + \bar{\bar{\tau}}\right)\cdot\bar{n}\,dS = \oint_{\partial\Omega} \overline{\overline{\sigma_n}}\cdot\bar{n}\,dS$$

where $p\bar{\bar{I}}$ represents the isotropic pressure component, $\bar{\bar{I}}$ being the unit tensor, and $\bar{\bar{\tau}}$ represents the *viscous stress tensor*:

$$\bar{\bar{\tau}} = \left(\overline{\tau_x}, \overline{\tau_y}, \overline{\tau_z}\right) = \begin{bmatrix} \tau_{xx} & \tau_{xy} & \tau_{xz} \\ \tau_{yx} & \tau_{yy} & \tau_{yz} \\ \tau_{zx} & \tau_{zy} & \tau_{zz} \end{bmatrix}$$

This notation, that refers to a Cartesian coordinates system, indicates that the particular stress component (τ_{ij}) acts along the j-axis direction and affects a plane whose normal is parallel to the i-axis. Thus, the terms on the tensor's diagonal represent the normal stresses, whilst the others represent the shear stresses.
The momentum conservation law can finally be written, in its integral formulation, as:

$$\frac{\partial}{\partial t}\int_{\Omega} \rho\bar{v}\,d\Omega + \oint_{\partial\Omega} (\rho\bar{v})\bar{v}\cdot\bar{n}\,dS = \int_{\Omega} \rho\bar{f_e}\,d\Omega - \oint_{\partial\Omega} p\bar{\bar{I}}\cdot\bar{n}\,dS + \oint_{\partial\Omega} \bar{\bar{\tau}}\cdot\bar{n}\,dS \qquad (3.2)$$

iii. Energy equation

The energy conservation law is based on the first law of thermodynamics. Considering the control volume of Figure 3.1, it states that total energy variations in this volume over time are due to the energy fluxes across the control surface and to the contribution of several source terms.
The total energy per unit mass (*E*) of a fluid is defined as the sum of its internal and

kinetic energy:

$$E = e + \frac{|\bar{v}|^2}{2}$$

The total energy variation over time within the control volume can therefore be written as:

$$\frac{\partial}{\partial t}\int_{\Omega} \rho E \, d\Omega$$

where *ρE* is the total energy per unit volume and represents the conserved quantity. Analogously to the previous cases, the energy flux across the control surface is:

$$-\oint_{\partial\Omega} (\rho E)\bar{v} \cdot \bar{n} \, dS$$

The source terms in this case are represented by the time rate of work done by the internal and external forces acting on the system and by the heat flux across the control surface. The first two terms can be expressed as, respectively:

$$\dot{L}_s = \oint_{\partial\Omega} (\overline{\overline{\sigma_n}} \cdot \bar{n}) \cdot \bar{v} \, dS$$

$$\dot{L}_v = \int_{\Omega} \rho \bar{f_e} \cdot \bar{v} \, d\Omega$$

The heat flux often includes the effect of molecular thermal conduction only. Using Fourier's law, it is written as:

$$\dot{Q}_s = \oint_{\partial\Omega} k\nabla T \cdot \bar{n} \, dS$$

where *k* is the thermal conductivity coefficient and *T* is the absolute static temperature. In some cases, heating due to the absorption or emission of radiations and to chemical reactions has to be considered as well. These further volumetric source terms are usually expressed as:

$$\dot{Q}_v = \int_{\Omega} \dot{q} \, d\Omega$$

The energy conservation law can finally be written, in its integral formulation, as:

$$\frac{\partial}{\partial t}\int_{\Omega} \rho E \, d\Omega + \oint_{\partial\Omega} (\rho E)\bar{v} \cdot \bar{n} \, dS =$$

$$= \oint_{\partial\Omega} (\overline{\overline{\sigma_n}} \cdot \bar{n}) \cdot \bar{v} \, dS + \int_{\Omega} \rho \bar{f_e} \cdot \bar{v} \, d\Omega + \oint_{\partial\Omega} k\nabla T \cdot \bar{n} \, dS + \int_{\Omega} \dot{q} \, d\Omega \quad (3.3a)$$

It is sometimes preferable to reformulate this equation introducing the total enthalpy per unit mass (*H*):

$$H = h + \frac{|\bar{v}|^2}{2} = E + \frac{p}{\rho}$$

After some manipulation, Equation (3.3a) becomes:

$$\frac{\partial}{\partial t}\int_{\Omega} \rho E \, d\Omega + \oint_{\partial\Omega} (\rho H)\bar{v} \cdot \bar{n} \, dS =$$

$$= \oint_{\partial\Omega} (\bar{\bar{\tau}} \cdot \bar{n}) \cdot \bar{v} \, dS + \int_{\Omega} \rho \bar{f_e} \cdot \bar{v} \, d\Omega + \oint_{\partial\Omega} k\nabla T \cdot \bar{n} \, dS + \int_{\Omega} \dot{q} \, d\Omega \quad (3.3b)$$

3.1.1. Navier-Stokes equations

For *Newtonian fluids*, such as water and air, viscous stresses can be expressed by the following relation:

$$\tau_{ij} = \mu\left(\frac{dv_i}{dx_j} + \frac{dv_j}{dx_i}\right) - \frac{2}{3}\mu\delta_{ij}\nabla \cdot \bar{v}$$

where v_i, v_j are the velocity components in Cartesian coordinates, μ is the dynamic viscosity and δ_{ij} is the *Kronecker delta*. If this hypothesis holds, Equations (3.1), (3.2) and (3.3b) can be re-written in an alternative form and are commonly known as *Navier-Stokes equations*. They describe the exchange of mass, momentum and energy through the boundary of an arbitrary control volume, which is fixed in space.
Navier-Stokes equations can also be written in compact form, as follows:

$$\frac{\partial}{\partial t}\int_{\Omega} W d\Omega + \oint_{\partial\Omega} \bar{F} \cdot \bar{n} \, dS = \int_{\Omega} Q d\Omega \quad (3.4)$$

Here, vector *W* contains the so-called *conservative variables*, and for a three-dimensional case reads:

$$W = \begin{bmatrix} \rho \\ \rho\bar{v} \\ \rho E \end{bmatrix}$$

where the velocity vector $\bar{v}$ consists of three components (*u*, *v*, *w*) with respect to the

Cartesian axes. Tensor $\bar{\bar{F}}$ represents the *flux tensor* and contains both the convective and diffusive terms. In three dimensions it can be expressed as:

$$\bar{\bar{F}} = \begin{bmatrix} \rho\bar{v} \\ (\rho\bar{v})\bar{v} + p\bar{\bar{I}} - \bar{\bar{\tau}} \\ \rho H\bar{v} - \bar{\bar{\tau}} \cdot \bar{v} - k\nabla T \end{bmatrix}$$

Lastly, vector Q contains the source terms, and can be written as:

$$Q = \begin{bmatrix} 0 \\ \rho\overline{f_e} \\ \rho\overline{f_e} \cdot \bar{v} + \dot{q} \end{bmatrix}$$

The compact formulation of the Navier-Stokes equations forms the basis of the numerical *finite volumes* method, which will be discussed in detail in a following section of this chapter. Applying Gauss's theorem, Equation (3.4) can also be re-written in differential form, which is the preferred option when turbulence modelling is concerned, as will be later explained.

For a three-dimensional case, the Navier-Stokes equations represent a system of five scalar equations, but contain seven unknown variables, namely the density (ρ), the three velocity components (u, v, w), the total energy per unit mass (E), the pressure (p) and the temperature (T): two additional thermodynamic relations are therefore required for closure. Expressions for the dynamic viscosity (μ) and the thermal conductivity coefficient (k) have to be provided as well. Apart from those cases where particular thermodynamic phenomena and chemical reactions are involved, it is reasonable to assume that the fluid behaves like a *perfect gas*, for which the equation of state can be formulated as:

$$\frac{p}{\rho} = \mathcal{R}T \quad (3.5)$$

where $\mathcal{R}$ is the specific gas constant. Furthermore, the following relation holds:

$$h = c_p T \quad (3.6)$$

where c_p is the specific heat of the gas at constant pressure. The dynamic viscosity for a perfect gas is strongly dependent on temperature, and can be determined using Sutherland's law:

$$\mu = \mu_{ref}\left(\frac{T}{T_{ref}}\right)^{1.5}\frac{T_{ref} + S}{T + S} \quad S = 110K \quad (3.7)$$

where μ_{ref} is the dynamic viscosity of the gas or liquid at the reference temperature (T_{ref}) and S is the Sutherland constant. The thermal conductivity coefficient is also dependent on the temperature for gases, whereas it is almost constant for liquids. The relation:

$$k = c_p \frac{\mu}{Pr} \quad (3.8)$$

where *Pr* is the Prandtl number, is commonly used for air. Equations (3.5)-(3.8) can therefore be applied as closure relations if the hypothesis of perfect gas holds true.

3.1.2. Euler equations

Navier-Stokes equations can be simplified for the case of an *ideal flow*, i.e. a flow where viscous and thermal effects can be neglected, and are known as *Euler equations*. They describe the pure convection of the flow quantities in an inviscid fluid. The compact form of the Euler equations is formally identical to Equation (3.4), but the flux tensor contains the convective terms only:

$$\bar{\bar{F}}_E = \begin{bmatrix} \rho\bar{v} \\ (\rho\bar{v})\bar{v} + p\bar{\bar{I}} \\ \rho H\bar{v} \end{bmatrix}$$

Euler equations form the basis for the development of a large variety of discretisation methods and boundary conditions, and their conservative formulation provides an accurate representation of several important phenomena, such as shocks and expansion waves.

3.2. Numerical solution of the governing equations

As explained in this chapter's introduction, the governing equations of fluid dynamics cannot be solved exactly, and numerical strategies are therefore needed in order to find approximate solutions for complex flow fields. Nearly all these methods follow the same key steps, which can be summarised as follows:

- The computational domain, i.e. the space where the flow field is to be computed, is divided into a certain number of geometrical entities, the so-called *cells*. This process is referred to as *grid* (or *mesh*) *generation*;
- The Navier-Stokes or Euler equations are discretised in space and time separately (*method of lines*), thus becoming algebraic relations, which can be solved by applying iterative processes;
- Initial and boundary conditions for the algebraic problem are defined.

Here, we will discuss about the first two steps, while the last step will be the subject matter of a following section.

3.2.1. Grid generation

Grids commonly consist of triangles or quadrilaterals for two-dimensional problems, whereas tetrahedral, hexahedra, prisms or pyramids are used in three-dimensional cases. Specific requirements are to be satisfied when the domain is discretised: first and foremost, cells must not overlap nor leave any “holes”; additionally, no abrupt changes in their volume or stretching ratio are allowed, and their shape should be as regular as possible, so as not to generate unacceptable numerical errors.
Grids can be generated to closely resemble the physical boundaries (*body-fitted grids*), as shown in Figure 3.2a, or to follow the Cartesian coordinates (*Cartesian grids)*, as shown in Figure 3.2b:

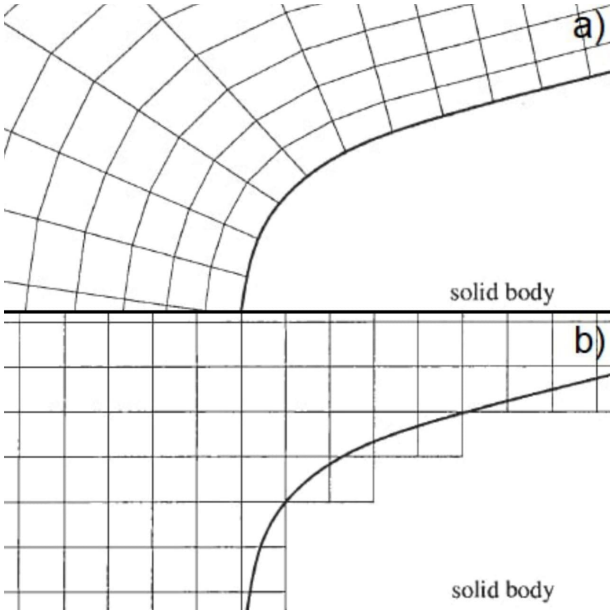

Figure 3.2. Body-fitted (top) and Cartesian (bottom) 2D grids

On the one hand, Cartesian grids are easily created and allow for a straightforward evaluation of the fluxes in Equation (3.4), but do not permit a rigorous treatment of the boundaries. On the other hand, body-fitted grids are adaptable to almost every geometry, and therefore accurately resolve boundaries, but are more complex to generate. Nowadays, the body-fitted approach is preferred, since in engineering applications boundaries are often geometrically elaborate.

Grids can furthermore be divided into *structured* and *unstructured* (Figure 3.3). In structured meshes, each grid point, called *vertex* or *node*, is uniquely defined by a certain number of indices (*i, j, k*) and the corresponding Cartesian coordinates, whereas in unstructured meshes cells and nodes do not have a particular order. Unstructured grids are also characterised by the presence of different types of cells, which are needed to accurately simulate the boundary layer: for this reason, they are sometimes called *hybrid* or *mixed* grids.

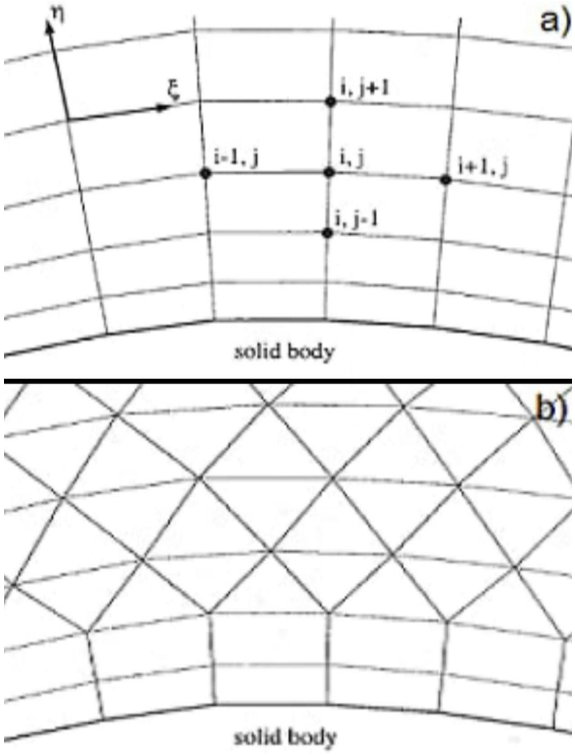

Figure 3.3. Structured (top) and mixed unstructured (bottom) 2D grids

In the present work, an unstructured mesh has been generated. This choice is motivated by the numerous advantages that this grid type offers: an unstructured mesh can deal with complex geometries with a significant reduction in cells number in comparison to the structured approach, and the time required for its creation is significantly lower. Moreover, *grid refinements* can be easily constructed.

Figure 3.4 shows the discretised computational domain for the test case of Nagashima et al.'s axisymmetric external compression air inlet model [1] in his *Spacer No. A* configuration. The grid has been realised with Gmsh, an open source mesh generator [21]: it contains approximately 107000 cells - mainly quadrangles - and has been created using the Frontal-Delaunay for Quads [22] and Blossom recombination [23] algorithms.

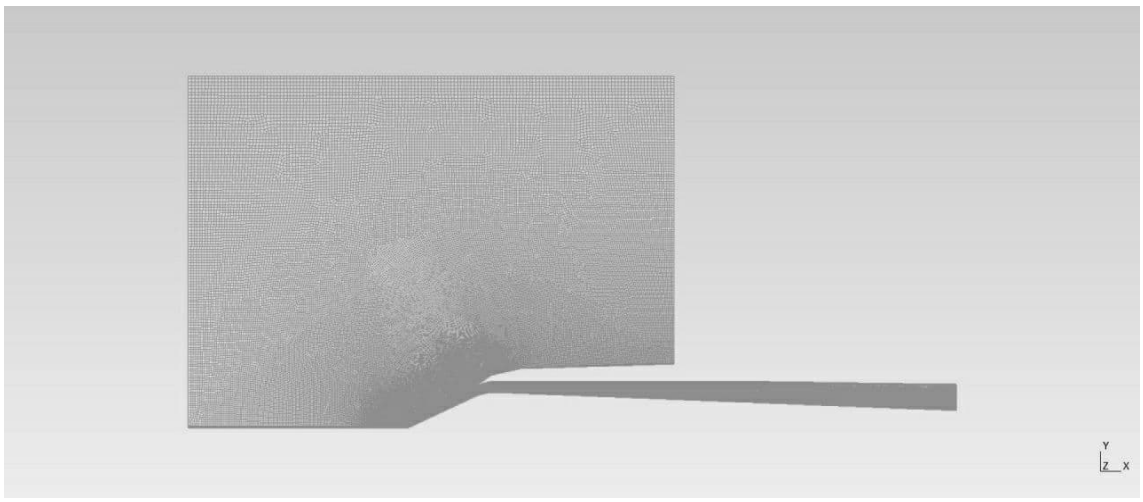

Figure 3.4. Computational domain and unstructured mesh for the air inlet model

It can be seen from Figure 3.4 that the mesh is refined in the areas over the compression ramp, around the cowl and in the duct, since the most important variations in the flow quantities are expected here, especially during subcritical operations (see Sections 2.3 and 2.6). Figure 3.5 shows the compression ramp refinement more clearly:

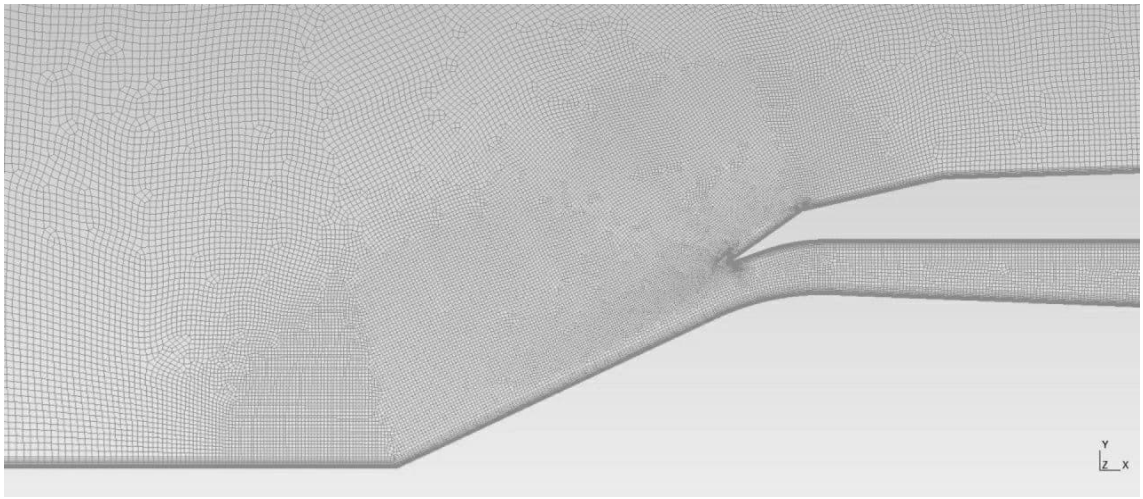

Figure 3.5. Compression ramp refinement

The boundary layers on the center body and on the cowl have been discretised using rectangular cells, which are orthogonal to the walls (Figure 3.6). The first cell's wall spacing has been determined for y^+=5, and a constant stretching ratio of 1.2 has been used. The boundary layer on the center body has been constructed using 18 layers, whereas the boundary layer on the cowl's inner and outer surfaces contains 16 layers.

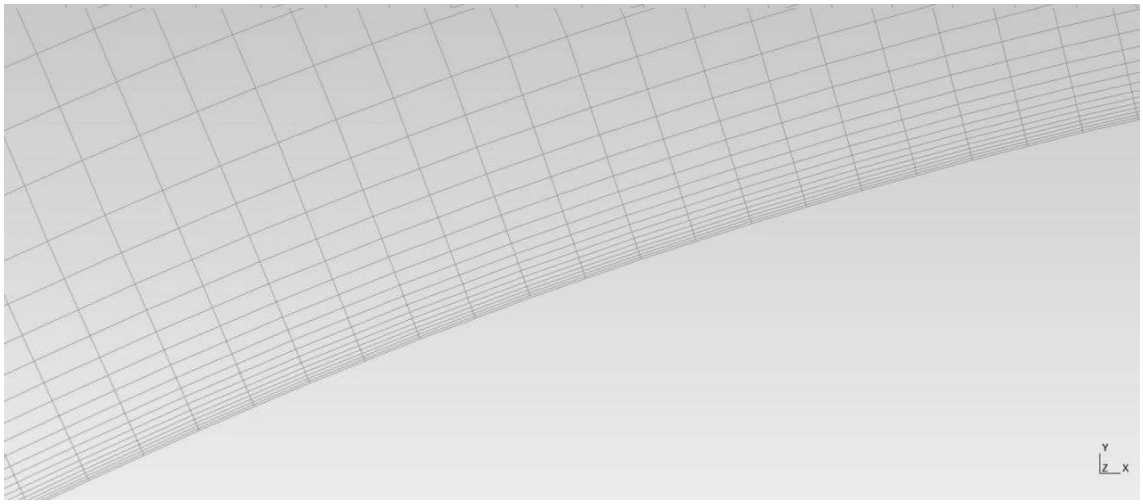

Figure 3.6. Boundary layer on the center body

Particular attention has been given to the sharp cowl lip, which has been discretised creating a mesh fan in the boundary layer (Figure 3.7):

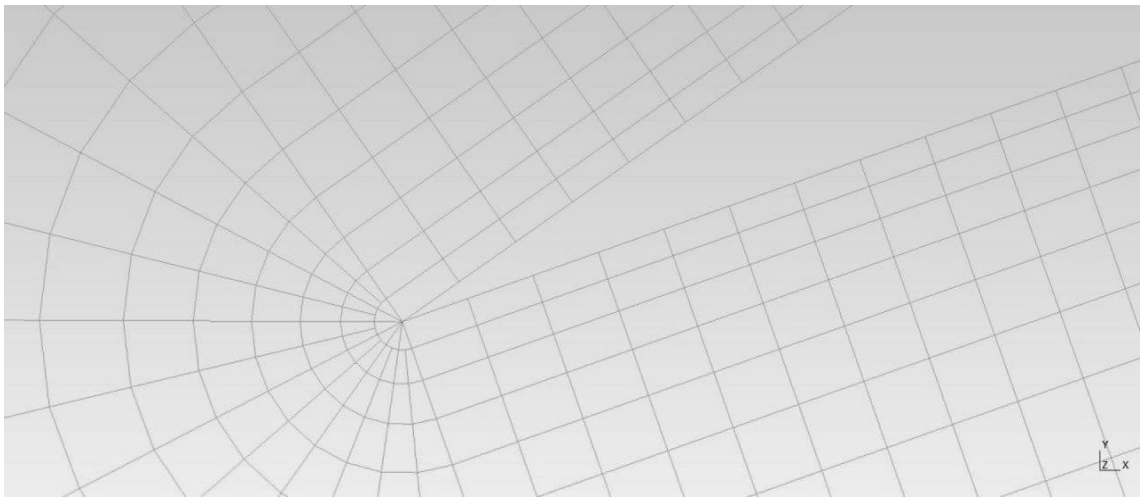

Figure 3.7. Cowl lip refinement

3.2.2. Finite volumes method

The second key step is the spatial and temporal discretisation of the governing equations. Three different methodologies can be chosen, namely *finite differences*, *finite volumes* and *finite elements*: in the present work, the finite volumes method has been implemented. This method is extremely flexible and can be utilised on both structured and unstructured grids: it is therefore suitable for the description of complex geometries. Moreover, since it is based on the conservative form of the governing equations, it guarantees that mass, momentum and energy are numerically conserved. This is not the case, for instance, when a finite difference scheme is implemented: in fact, substitutive relations, namely the *Rankine-Hugoniot relations*, have to be locally used to resolve discontinuities in such schemes. This represents an enormous

advantage of the finite volumes method.

As anticipated in Section 3.1.1, the finite volumes method is based on the compact integral formulation of the Navier-Stokes equations (Equation (3.4)), which are discretised by first dividing the domain into a certain number of *control volumes*. There exist two main possibilities for the definition of each control volume's shape and position: the *cell-centred* scheme (Figure 3.8a), in which the flow quantities are stored at the centroids of the grid cells, and the *cell-vertex* scheme (Figure 3.8b), in which the flow quantities are stored at the grid points. Thus, the control volumes are identical to the cells for a cell-centred scheme, whilst they can either be the union of all the cells that share the grid point (*overlapping control volumes*) or some particular volumes defined around the grid points (*dual control volumes*) for a cell-vertex scheme. A cell-centred scheme has been chosen for our discretisation process.

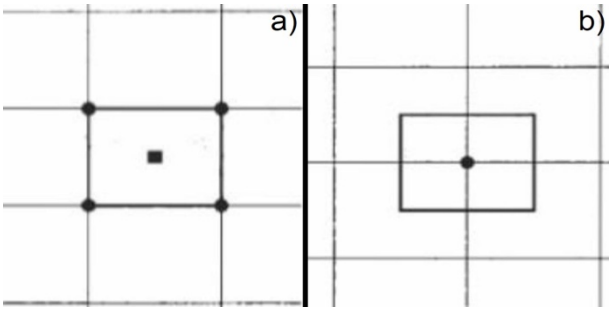

Figure 3.8. Cell-centred (left) and dual control volumes cell-vertex (right) schemes

Equation (3.4) is then applied to each control volume (Ω_i) individually, and reads:

$$\frac{\partial}{\partial t}\int_{\Omega_i} W d\Omega + \oint_{\partial\Omega_i} \bar{F}\cdot\bar{n}\, dS = \int_{\Omega_i} Q d\Omega \qquad (3.9)$$

The volume integral of the conservative variables vector (W) can be approximated introducing a *mean value*:

$$W_i = \frac{1}{\Omega_i}\int_{\Omega_i} W d\Omega$$

Analogously, the source terms vector (Q) becomes:

$$Q_i = \frac{1}{\Omega_i}\int_{\Omega_i} Q d\Omega$$

The surface integral can be split into the sum of the fluxes across the control volume's faces:

$$\oint_{\partial\Omega_i} \bar{F} \cdot \bar{n}\, dS = \sum_{faces} \int_{face} \bar{F} \cdot \bar{n}\, dS$$

and, for sufficiently small volumes, the flux across each face is supposed to be constant. This hypothesis allows us to introduce another approximation:

$$\sum_{faces} \int_{face} \bar{F} \cdot \bar{n}\, dS = \sum_{faces} \bar{F} \cdot \bar{n}\, \Delta S$$

where ΔS is the area of the particular face, $\bar{n}$ being its unit normal vector. Finally, Equation (3.9) becomes:

$$\frac{\partial}{\partial t}(\Omega_i W_i) + \sum_{faces} \bar{F} \cdot \bar{n}\, \Delta S = \Omega_i Q_i \quad (3.10)$$

Equation (3.10) represents the general expression on which the finite volumes schemes are based. It describes the evolution of the mean conservative variables (W_i) over time as a function of the fluxes across the volume's faces ($\bar{F}$) and the source terms (Q_i). Under the assumption that the control volumes do not change with time, Equation (3.10) can furthermore be reformulated as:

$$\Omega_i \frac{\partial W_i}{\partial t} + \sum_{faces} \bar{F} \cdot \bar{n}\, \Delta S = \Omega_i Q_i \quad (3.11)$$

The crucial aspect of the finite volumes method is the evaluation of the convective fluxes at all faces of each control volume; however, since the flow variables are not univocally defined here, interpolation strategies are needed. There are several ways to obtain the fluxes at a cell face for a cell-centred scheme:

- by an average of the fluxes evaluated at the centroids of the cells adjacent to the face;
- by an average of the conservative variables associated with the centroids of the cells adjacent to the face;
- by considering the fluxes as a function of the flow variables associated with the centroid of only one of the cells adjacent to the face, taking the characteristics of the equations into consideration.

Depending on the adopted spatial discretisation strategy, the resulting finite volumes scheme will be identified as *central* or *upwind*. The central schemes require less CPU time per evaluation in comparison to the upwind schemes, but are characterised by an

intrinsic instability, which has to be suppressed with the introduction of the so-called *artificial dissipation*. The upwind schemes, on the other hand, are constructed by considering the physical properties of the Euler equations - which contain the convective terms only (see Section 3.1.2) - and distinguish between upstream and downstream signal propagation directions, thus being more costly. Nonetheless, due to their reduced *numerical diffusion*, they are able to describe flow discontinuities more accurately than the central schemes, and can resolve boundary layers using less grid points. An extremely important problem arises, however, when a second or higher order spatial accuracy is required for an upwind scheme: in these cases, *limiter functions* must be implemented in order to avoid spurious oscillations near flow discontinuities, with negative consequences on the convergence and on the computational effort, especially for unstructured grids. In the present work, a second-order accuracy upwind scheme with the Barth and Jespersen limiter [24] has been used. Barth's limiter enforces a monotone solution in the presence of discontinuities, but tends to smear them and is somewhat dissipative. Furthermore, it is activated by numerical noise in smooth flow regions, thus preventing the full convergence to the steady state in some problems.

Besides fluxes evaluation, the time derivative in Equation (3.11) has to be approximated as well. Temporal discretisation techniques are based on the idea of time as a series of discrete *time steps*: applying the definition of derivative as rate of change and using Taylor expansions, different first or second-order accurate schemes can be obtained. Once the time derivative has been substituted by an algebraic expression, the temporal instant at which the fluxes and source terms are evaluated has to be chosen. In order to dilate upon this fundamental decision, let us consider two successive instants, namely t^k and t^{k+1}: if the fluxes and source terms in the discretised equation are calculated considering the flow variables evaluated at t^k, the scheme is called *explicit*; on the other hand, if these quantities are evaluated at t^{k+1}, the scheme is said to be *implicit*. Explicit schemes are numerically economical, but the maximum allowable time step is severely limited by stability restrictions, thus significantly slowing down the convergence to the steady state in some simulations, although several acceleration techniques are nowadays implemented to partially overcome this limitation [25], [26], [27]. Implicit schemes, on the other hand, permit to select larger time steps without affecting the stability of the method; moreover, they are faster and more robust than explicit schemes in many cases. However, computational costs are considerably higher, due to the fact that a system of linear algebraic equations has to be solved at each temporal instant using an iterative strategy. The decision whether to use an implicit or explicit scheme is therefore dependent on the particular problem as well as

on the fluid dynamicist's necessities. A first-order accurate implicit scheme has been implemented for our near-critical case simulations, whereas a second order implicit scheme has been used for the investigation of the subcritical operating conditions.

As explained above, the time step in CFD simulations cannot be selected arbitrarily, but has to be determined in order to meet the method's stability requirements. This particularly applies to explicit schemes, where the so-called *Courant-Friedrichs-Lewy* (*CFL*) condition [28] must be satisfied. It states that the domain of dependence of the numerical method must contain the physical domain of dependence, i.e. the domain of dependence of the differential equation. Such condition is easily expressed for the one-dimensional linear scalar advection equation:

$$\frac{\partial u}{\partial t} + a\frac{\partial u}{\partial x} = 0 \quad (3.12)$$

as:

$$\sigma = |a|\frac{\Delta t}{\Delta x} \leq \sigma_{max} \quad (3.13)$$

where Δt is the time step, Δx is the cell size and a is the velocity at which the quantity u is transported. σ is the *CFL* or *Courant number* and is always positive, and σ_{max} is a limit value determined by the *von Neumann* stability analysis. The stability condition is thus translated into a limitation to the Courant number's values: depending on the scheme that has been used, different values of σ may be chosen. The time step is consequently obtained from the inverse formula of (3.13). Nevertheless, for more complex cases, such as the non-linear Navier-Stokes equations system, finding an expression for the stability condition is not straightforward, since it is strongly dependent on the implemented scheme. For this reason, the time step cannot be calculated exactly, but has to be determined empirically: its selection therefore becomes an engineering judgement. This holds true for implicit schemes as well, but the restrictions on the Courant number values are less severe. In the present work, a variable CFL number, ranging between 5 and 100, has been used for the treatment of the near-critical case, whilst a constant CFL number σ=5 has been selected for the subcritical regime simulations.

3.3. Turbulence and its modelling

Most of the fluid dynamics phenomena encountered in engineering applications are *turbulent*. Turbulent flows are characterised by a quasi-random and chaotic behaviour, and are intrinsically unsteady: all the flow variables vary with time in an a somewhat

arbitrary manner (Figure 3.9).

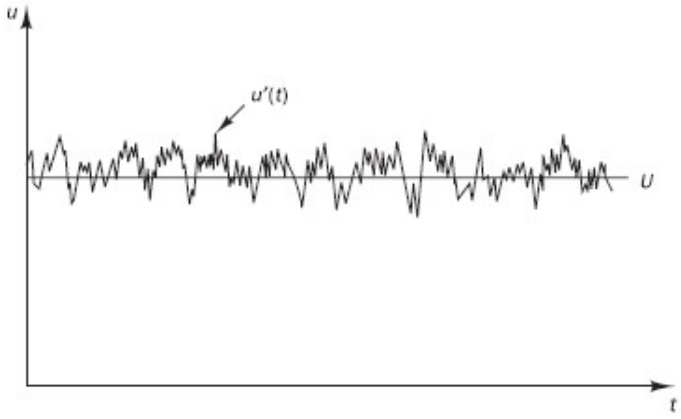

Figure 3.9. Typical point velocity measurement in a turbulent flow

Turbulent flows are furthermore three-dimensional and multi-scale phenomena, since the typical rotational structures, called *turbulent eddies* (Figure 3.10), are associated with a wide range of different length scales. Turbulent eddies interact in a dynamically complex way: an economical description of every fluid particle's motion is therefore often unachievable.

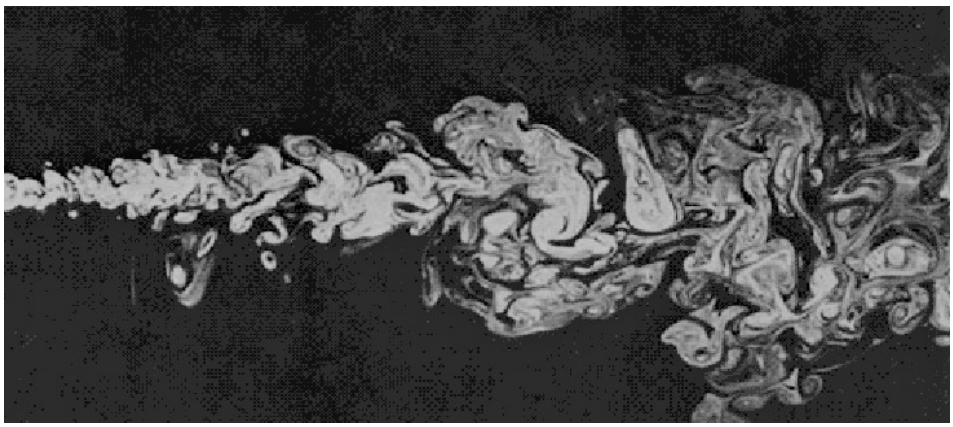

Figure 3.10. Turbulent eddies visualisation

3.3.1. Reynolds and Favre decompositions

For the aforesaid reasons, a simplified approach to turbulence is frequently used, in which the flow variables are seen as the sum of a mean value and a fluctuation about it: this strategy is known as *Reynolds decomposition*. Figure 3.9 shows the Reynolds decomposition of the velocity (*u(t)*) into its steady mean value (*U*) and a superimposed fluctuating component (*u'(t)*). Generalising, an arbitrary scalar or vector flow quantity (φ) can be written as:

$$\varphi = \bar{\varphi} + \varphi' \quad (3.12)$$

If the mean flow is steady, the mean value ($\bar{\varphi}$) in (3.12) is defined as:

$$\bar{\varphi} = \lim_{T\to\infty} \frac{1}{T} \int_{t}^{t+T} \varphi \, dt$$

This process is called *time averaging*. On the other hand, if the mean flow is time-dependent, the mean value ($\bar{\varphi}$) has to be determined using an *ensemble average*:

$$\bar{\varphi} = \lim_{N\to\infty} \frac{1}{N} \sum_{i=1}^{N} \varphi_i$$

and still remains a function of time and space. The fluctuations (φ') are therefore defined as:

$$\varphi' = \varphi - \bar{\varphi}$$

and their average is always null. The spread of fluctuations about the mean value is described by the *variance* and the *root mean square* (*rms*), respectively defined as:

$$\overline{(\varphi')^2} = \frac{1}{\Delta t} \int_{0}^{\Delta t} (\varphi')^2 \, dt$$

$$\varphi_{rms} = \sqrt{\overline{(\varphi')^2}} = \sqrt{\frac{1}{\Delta t} \int_{0}^{\Delta t} (\varphi')^2 \, dt}$$

The variance is alternatively called *second moment* of the fluctuations. It can also be defined when two different variables (φ and ψ) are considered:

$$\overline{\varphi'\psi'} = \frac{1}{\Delta t} \int_{0}^{\Delta t} \varphi'\psi' \, dt$$

Since in turbulent flows the velocity fluctuations in different directions (*u'*, *v'*, *w'*) are not independent, the second moments obtained considering their products are non-zero, and contain important information on the flow physics, as will be later explained.
When the flow density is not constant, the Reynolds averaging is usually combined with another decomposition, known as *Favre averaging* [29]:

$$\theta = \tilde{\theta} + \theta'' \quad (3.13)$$

where θ can be either a scalar or a vector quantity. $\tilde{\theta}$ represents the mean value, while θ'' indicates the fluctuating part, analogously to the Reynolds decomposition. The mean value for Favre-average quantities is defined as:

$$\tilde{\theta} = \frac{1}{\bar{\rho}} \lim_{T\to\infty} \frac{1}{T} \int_{t}^{t+T} \rho\theta \, dt$$

where the overbar indicates the Reynolds-averaged density.

3.3.2. Favre- and Reynolds-Averaged Navier-Stokes equations

Following the Reynolds and Favre decompositions approach, the Navier-Stokes equations (Equation (3.4)) can be re-written and averaged in order to obtain a new system of equations, known as *Favre- and Reynolds-Averaged Navier-Stokes* (*RANS*) *equations*, which describe the effects of turbulence on the mean flow properties for compressible flows. Considering a Cartesian coordinates system, they read[1]:

$$\frac{\partial \bar{\rho}}{\partial t} + \nabla \cdot (\bar{\rho}\tilde{\boldsymbol{v}}) = 0 \quad (3.14)$$

$$\frac{\partial (\bar{\rho}\tilde{u})}{\partial t} + \nabla \cdot (\bar{\rho}\tilde{u}\tilde{\boldsymbol{v}}) = = -\frac{\partial \bar{p}}{\partial x} + \nabla \cdot (\mu \nabla \tilde{u}) + \left[-\frac{\partial (\widetilde{\bar{\rho}u''^2})}{\partial x} - \frac{\partial (\widetilde{\bar{\rho}u''v''})}{\partial y} - \frac{\partial (\widetilde{\bar{\rho}u''w''})}{\partial z} \right] + Q_{M,x} \quad (3.15a)$$

$$\frac{\partial (\bar{\rho}\tilde{v})}{\partial t} + \nabla \cdot (\bar{\rho}\tilde{v}\tilde{\boldsymbol{v}}) = = -\frac{\partial \bar{p}}{\partial y} + \nabla \cdot (\mu \nabla \tilde{v}) + \left[-\frac{\partial (\widetilde{\bar{\rho}u''v''})}{\partial x} - \frac{\partial (\widetilde{\bar{\rho}v''^2})}{\partial y} - \frac{\partial (\widetilde{\bar{\rho}v''w''})}{\partial z} \right] + Q_{M,y} \quad (3.15b)$$

$$\frac{\partial (\bar{\rho}\tilde{w})}{\partial t} + \nabla \cdot (\bar{\rho}\tilde{w}\tilde{\boldsymbol{v}}) = = -\frac{\partial \bar{p}}{\partial z} + \nabla \cdot (\mu \nabla \tilde{w}) + \left[-\frac{\partial (\widetilde{\bar{\rho}u''w''})}{\partial x} - \frac{\partial (\widetilde{\bar{\rho}v''w''})}{\partial y} - \frac{\partial (\widetilde{\bar{\rho}w''^2})}{\partial z} \right] + Q_{M,z} \quad (3.15c)$$

$$\frac{\partial (\bar{\rho}\tilde{\varphi})}{\partial t} + \nabla \cdot (\bar{\rho}\tilde{\varphi}\tilde{\boldsymbol{v}}) = \nabla \cdot (\Gamma_{\Phi} \nabla \tilde{\varphi}) + \left[-\frac{\partial (\widetilde{\bar{\rho}u''\varphi''})}{\partial x} - \frac{\partial (\widetilde{\bar{\rho}v''\varphi''})}{\partial y} - \frac{\partial (\widetilde{\bar{\rho}w''\varphi''})}{\partial z} \right] + Q_{\Phi} \quad (3.16)$$

where the energy equation has been substituted by a transport equation for a generic scalar quantity (φ). Here, ρ is the flow density, p is the pressure, $\boldsymbol{v}$ is the velocity vector, whose components are u, v and w, and u'', v'' and w'' are the velocity fluctuations. Q_M and Q_Φ are generic source terms. The overbar indicates a Reynolds-averaged variable, whereas the tilde indicates a Favre-averaged quantity.

Equations (3.14)-(3.16) are formally similar to the Navier-Stokes equations, but the averaging process has introduced new terms in the momentum and scalar transport equations: these terms, grouped in square brackets, involve the product of fluctuating velocities, and represent the convective momentum and scalar quantity transport due to turbulent eddies. With respect to the momentum equation, these terms are called *Reynolds stresses*, since they act as additional turbulent stresses on the mean velocity components. They are usually large in comparison to the viscous stresses, and

[1] As anticipated in Section 3.1.1, the equations are written in differential form, which is usually preferred to the integral formulation when turbulence modelling is discussed, since it allows the notation to be compact and clear.

therefore have a dominant effect on the flow field - except for an extremely small region near the body, as we will later see. The Reynolds stresses and the turbulent scalar transport terms represent additional unknowns in the RANS equations, and cause the system to be non-closed: for this reason, they have to be mathematically modelled. The so-called *RANS turbulence models* are commonly classified according to the number of additional transport equations that need to be solved together with Equations (3.14)-(3.16), as shown in Table 3.1, and are characterised by different ranges of applicability, degrees of accuracy and computational costs.

Number of extra equations	Turbulence model
0	Mixing length model
1	Spalart-Allmaras
2	k-ε, k-ω, Algebraic stress model
7	Reynolds stress model

Table 3.1. RANS turbulence models

3.3.3. Turbulent flows near solid walls

Before discussing turbulence models in more detail, we shall describe the characteristics of turbulent flows near solid walls, since the presence of such boundaries strongly influences the flow's structure and behaviour.

Let us consider the simplified case of a uniform air flow (ρ=1.225 kg/m^3, μ=1.84×10^{-5} Pa·s) over a flat plate, whose characteristic length is L=1.0 m, with no angle of attack. If the mean flow velocity is U=10 m/s, the Reynolds number based on the characteristic length is:

$$Re_L = \frac{\rho U L}{\mu} \approx 6.7 \times 10^5$$

above the critical value Re_{crit}=10^5 at which the transition from laminar to turbulent flow takes place. This implies that the inertial forces are much larger than their viscous counterpart. On the other hand, the Reynolds number based on the distance from the wall (y), defined as:

$$Re_y = \frac{\rho U y}{\mu}$$

varies with the coordinate y, and can therefore be greater than Re_{crit} if the distance from the wall is large enough, but also tend to zero for sufficiently small values of y. In the latter case, the viscous forces are of the same magnitude or even larger than the

inertial forces: this means that, in turbulent flows along solid bodies, there is a thin region, inside the boundary layer, where viscous effects are important, while inertia is dominant everywhere else.

The turbulent boundary layer is divided into two particular regions, namely *the inner layer* and the *outer layer*. Introducing two new dimensionless variables:

$$y^+ = \frac{yu_\tau}{\nu}$$

$$u^+ = \frac{U}{u_\tau}$$

where:

$$u_\tau = \sqrt{\frac{\tau_w}{\rho}}$$

is the *friction velocity*, and:

$$\nu = \frac{\mu}{\rho}$$

is the kinematic viscosity, dimensional analysis shows that the flow variables in the inner layer do not depend on any free stream parameters, and that the mean velocity is a function of y, ρ, μ and τ_w only, the last quantity being the *wall shear stress*. Thus:

$$u^+ = f(y^+) \quad (3.17)$$

Relation (3.17) is called *law of the wall*. The inner layer can furthermore be divided into three sub-layers, namely the *viscous*, *buffer* and *logarithmic* layers. The viscous sublayer, as the name implies, is dominated by viscous effects, and is characterised by a linear relationship between the dimensionless variables:

$$u^+ = y^+ \quad (3.18a)$$

This relation is valid for $0 \leq y^+ \leq 5$. The logarithmic layer is, on the other hand, dominated by the Reynolds stresses. Here, a logarithmic relationship between u^+ and y^+ holds:

$$u^+ = \frac{1}{k}\ln(y^+) + C \quad (3.18b)$$

where $k \approx 0.41$ is the von Karman constant and $C \approx 5$ is the Coles constant. Relation (3.18b) is valid for $30 \leq y^+ \leq 100$ and is often referred to as *log-law*. Outside the logarithmic layer, i.e. in the outer layer, where inertial effects prevail, the law of the wall

is not valid and has to be substituted by the so-called *law of the wake*:

$$\frac{U_e - U}{u_\tau} = -\frac{1}{k}\ln\left(\frac{y}{\delta}\right) + A \quad (3.19)$$

where U_e is the mean external flow velocity, δ is the boundary layer total thickness and A is a constant. Relationships (3.18a), (3.18b) and (3.19) are usually plotted on a semi-logarithmic diagram (Figure 3.11):

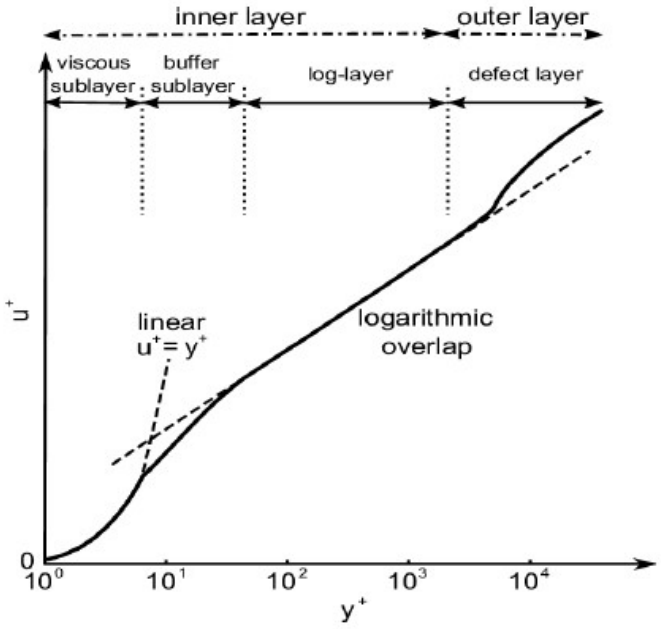

Figure 3.11. Law of the wall and law of the wake

The multi-layer structure is a universal feature of turbulent boundary layers near solid surfaces.

3.3.4. The Boussinesq hypothesis

As explained above, momentum transfer in a turbulent flow is mainly due to the action of the eddies, especially the largest and most energetic ones. In 1877 Boussinesq formulated an important hypothesis, based on this observation, in which he stated that the turbulent shear stress and the mean rate of strain are linearly related, analogously to laminar flows, and that the proportionality factor is represented by the so-called *turbulent* or *eddy viscosity* (μ_t) [30]. The eddy viscosity does not represent any physical characteristics of the fluid: in fact, it is a function of the local flow conditions and is affected by "flow history" effects.

For the Favre- and Reynolds-Averaged Navier-Stokes equations, this hypothesis reads:

$$-\bar{\rho}\widetilde{v_i''v_j''} = 2\mu_t\tilde{S}_{ij} - \delta_{ij}\frac{2}{3}\mu_t\frac{\partial\tilde{v}_k}{\partial x_k} - \delta_{ij}\frac{2}{3}\bar{\rho}\widetilde{K}$$

where $\tilde{S}_{ij}$ and $\widetilde{K}$ are the Favre-averaged strain rate and turbulent kinetic energy respectively. By applying the Boussinesq hypothesis to Equations (3.15a), (3.15b) and (3.15c), the dynamic viscosity (μ) is thus replaced by the sum of a laminar and a turbulent contribution:

$$\mu = \mu_l + \mu_t$$

where the laminar viscosity can be determined, for example, using the well-known Sutherland formula (Equation (3.7)).

By analogy, the turbulent transport of the scalar quantity in Equation (3.16) is assumed to be proportional to the gradient of its mean value:

$$-\bar{\rho}\widetilde{u_i''\varphi''} = \Gamma_t\frac{\partial\tilde{\varphi}}{\partial x_i}$$

where Γ_t represents the *eddy diffusivity*. Its value is close to that of the eddy viscosity, since the transport of the scalar quantity is also dominated by the action of the eddies: this assumption is known as *Reynolds analogy*. The ratio between eddy viscosity and eddy diffusivity is called *Schmidt number*:

$$\sigma_t = \frac{\mu_t}{\Gamma_t}$$

and is often approximated as constant and equal to unity in CFD solvers.

Despite several limitations, mainly caused by the assumption of equilibrium between the turbulence and the mean strain field, the Boussinesq hypothesis is adopted by a large variety of turbulence models, since it only requires the determination of the eddy viscosity.

3.3.5. The Spalart-Allmaras model

As anticipated in Section 3.3.2, turbulence models are necessary for the closure of the RANS equations system (Equations (3.14)-(3.16)). They are able to predict the Reynolds stresses and the scalar transport terms, and form the basis of the turbulence calculation procedures implemented in numerous modern CFD codes.

In the present work, the *Spalart-Allmaras* model has been used [31]. It involves one transport equation for the *kinematic eddy viscosity parameter* ($\tilde{\nu}$) and provides the definition of a length scale through an algebraic formula.

The kinematic eddy viscosity parameter is related to the eddy viscosity (μ_t) by the

relationship:

$$\mu_t = \rho\tilde{\nu} f_{v1}$$

where f_{v1} is a *wall damping function* which tends to unity for high Reynolds numbers, so that the kinematic eddy viscosity parameter is equal to the kinematic eddy viscosity (ν_t), and tends to zero at the wall. Following the Boussinesq hypothesis, the Reynolds stresses in Equations (3.15a), (3.15b) and (3.15c) are therefore computed as:

$$-\bar{\rho}\widetilde{v_i''v_j''} = 2\mu_t\tilde{S}_{ij} = \rho\tilde{\nu} f_{v1}\left(\frac{\partial\tilde{u}_i}{\partial x_j} + \frac{\partial\tilde{u}_j}{\partial x_i}\right)$$

The differential form of the transport equation for the kinematic eddy viscosity parameter reads:

$$\frac{\partial(\rho\tilde{\nu})}{\partial t} + \nabla\cdot(\rho\tilde{\nu}\tilde{\boldsymbol{v}}) = \frac{1}{\sigma_v}\nabla\cdot\left[(\mu+\rho\tilde{\nu})\nabla(\tilde{\nu}) + C_{b2}\rho\frac{\partial\tilde{\nu}}{\partial x_k}\frac{\partial\tilde{\nu}}{\partial x_k}\right] + C_{b1}\rho\tilde{\nu}\tilde{\Omega} - C_{w1}\rho\left(\frac{\tilde{\nu}}{ky}\right)^2 f_w \quad (3.20)$$

or, in words:

$$\begin{matrix}\text{Rate of}\\ \text{change of } \tilde{\nu}\end{matrix} + \begin{matrix}\text{Transport}\\ \text{of } \tilde{\nu} \text{ by}\\ \text{convection}\end{matrix} = \begin{matrix}\text{Transport}\\ \text{of } \tilde{\nu} \text{ by}\\ \text{turbulent diffusion}\end{matrix} + \begin{matrix}\text{Rate of}\\ \text{production}\\ \text{of } \tilde{\nu}\end{matrix} - \begin{matrix}\text{Rate of}\\ \text{dissipation}\\ \text{of } \tilde{\nu}\end{matrix}$$

The rate of production of $\tilde{\nu}$ is related to the local mean vorticity (Ω) by the relationship:

$$\tilde{\Omega} = \Omega + \frac{\tilde{\nu}}{(ky)^2} f_{v2}$$

The functions f_{v2} and f_w are further wall damping functions, and σ_v, k, C_{b1}, C_{b2} and C_w are model constants. These parameters are usually determined by *best practices*. The term ky, where y represents the distance from the solid wall, is used as the length scale and is equal to the mixing length assumed to derive the log-law presented in Section 3.3.3 (Equation (3.18b)).

The Spalart-Allmaras model provides economical and accurate computations of turbulent boundary layers in external aerodynamics applications, especially where adverse pressure gradients are present, and is capable of describing the transition from laminar to turbulent flow smoothly. It is a *local* model, i.e. the solution of Equation (3.20) at one point in the flow field does not depend on the solution at other points: for this reason, it can be implemented on both structured and unstructured grids. The Spalart-Allmaras model is furthermore robust, fast-converging and requires moderate grid resolutions in the region near the solid wall. On the other hand, it is somewhat insensitive to transport processes in rapidly changing flows and is generally

inappropriate for the description of internal flows.

3.4. Determination of initial and boundary conditions

When implementing a finite volumes scheme for the resolution of the Navier-Stokes equations, Equation (3.11) must hold for all the control volumes (Ω_i) into which the domain is divided. Thus, a system of ordinary differential equations (ODEs), hyperbolic with respect to time, is obtained, and a known *initial solution* is needed in order to advance in time. Such solution defines the state of the fluid at the first step of the iterative scheme, and can be determined following several different approaches: in external aerodynamics applications, for instance, a uniform initial condition is usually prescribed, and the free-stream values of the flow variables are assigned to all the control volumes; in numerous turbomachinery applications, on the other hand, it is preferable to specify the flow direction in the domain, and physically meaningful initial conditions are usually generated. In the present work, a uniform initial condition has been defined, and an initial Mach number M_{init}=2 has been assigned to the entire flow field. The Reynolds number has been set to $Re \approx 1.0 \times 10^7$, in accordance with the experimental data.

In addition to the initial solution, the so-called *boundary conditions* must be determined, since computational processes cannot afford to simulate the entire physical domain, which in turn has to be truncated, thus generating "artificial" boundaries at which some flow quantities need to be defined. Bearing in mind that the computed solution should be as accurate as possible, however, these boundaries are usually located at a distance from the object of the investigation, so as not to interfere with the structure of the flow field in the critical areas. Clearly, an exception to this rule is represented by the object's walls. The numerical treatment of these conditions requires particular attention, as an improper implementation would lead to erroneous results, and may influence the scheme's stability and convergence speed. Moreover, depending on the type of boundary condition - i.e. depending on the area of the flow field that they simulate numerically - and on the selected scheme, different discretisation techniques have to be used. With respect to Figure 3.12, the following boundary conditions have been implemented in the present work: *AB* is a supersonic inlet, where the free-stream Mach number (M_{inlet}), reference total pressure (p^0_{ref}) and reference total temperature (T^0_{ref}) values have been specified; *CD* is a supersonic outlet, while *EF* is a subsonic outlet, where the value of the local normalised mean static pressure ($p_n=p_s/p^0_{ref}$) has been set; *BC* and *AG* are symmetry planes, since there is no angle of attack (α) between the flow direction and the inlet's axis; finally, all the remaining boundaries are solid walls, where a *no-slip* condition has been imposed.

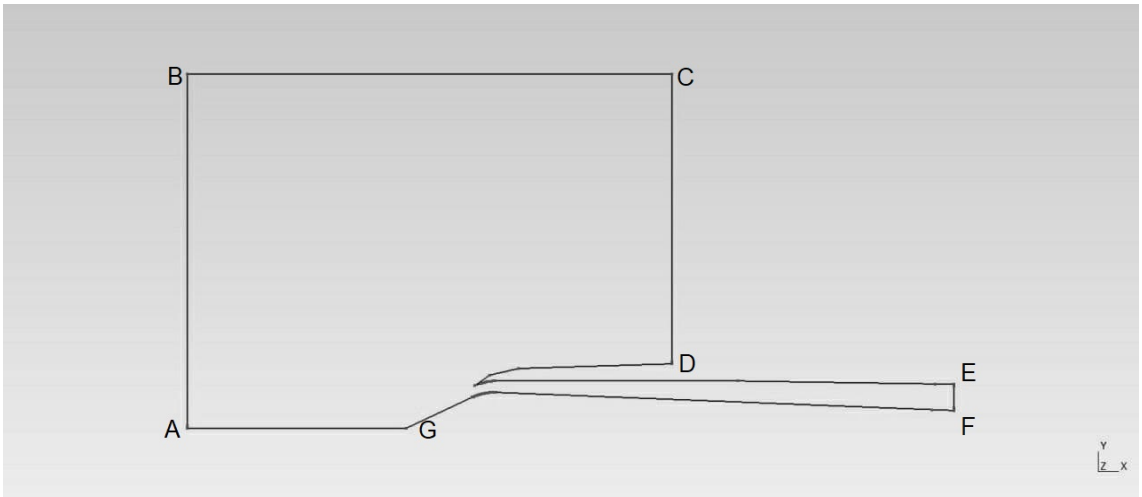

Figure 3.12. Computational domain and boundaries

The selected initial and boundary conditions are summarised in Table 3.2:

Parameter	Value
M_{init}	2.0
Re	1.0×10^{7}
M_{inlet}	2.0
p^{0}_{ref}	3 [atm]
T^{0}_{ref}	271.36 [K]
p_n	variable
α	0 [deg]

Table 3.2. Initial and boundary conditions

Note that the normalised static pressure in Table 3.2 is specified as variable because, depending on its values, different operating regimes can be simulated, as will be shown in Chapter 4.

4. Results and discussion

In this chapter, the results of our numerical simulations will be discussed in detail and compared with Nagashima et al.'s experimental findings [1], as well as with several solutions obtained in other computational studies.
The flow field images have been generated with VisIt, an open source visualisation, animation and analysis tool [32].

4.1. Near-critical case (TR=1.42)

The first case concerns a *near-critical*, steady-state operating condition, identified in Nagashima's work by a *throttle ratio* value *TR*=1.42, corresponding to a normalised static pressure $p_n \approx 0.65$ at the subsonic outlet of our computational domain (see Section 3.4). This configuration has also been investigated numerically by Newsome [12].
Figure 4.1 shows the Mach number distribution over the flow field. The represented shock waves system is typical of the supercritical regime: indeed, the presence of an oblique shock, generated from the ramp tip and propagating downstream, and a terminal shock, located within the duct, can be observed (see Section 2.3).

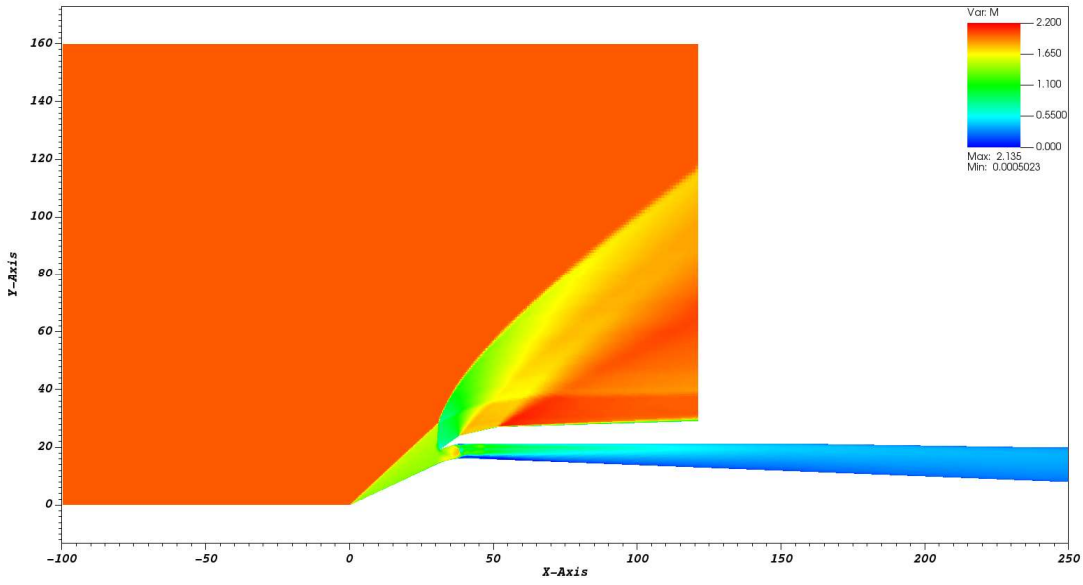

Figure 4.1. Mach number distribution (TR=1.42)

Figure 4.2 illustrates the internal flow's structure more clearly, and highlights the interaction between the shock wave and the boundary layer, which separates on the center body and the cowl as a result of the local high adverse pressure gradients. Such interaction causes the expected single normal shock to be substituted by multiple weak shocks, as already suggested by Newsome: the Mach number consequently oscillates

around unity in the initial part of the divergent duct before decreasing to subsonic values.

The interaction between the external oblique shock and another shock, generated from the sharp cowl lip, can furthermore be noticed. The resulting discontinuity is subsequently weakened by the two expansion fans that originate from the cowl's external surface.

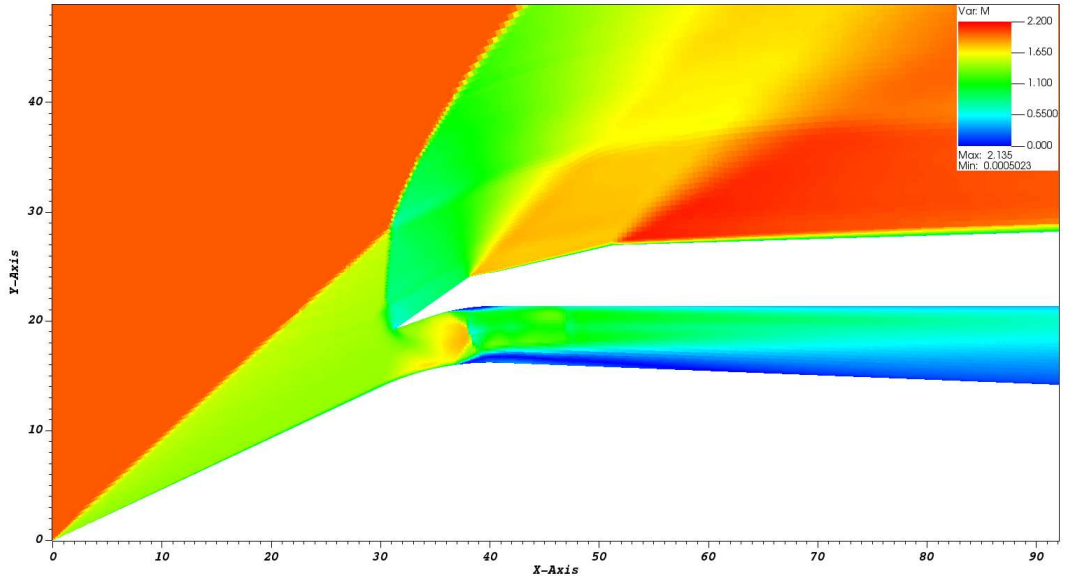

Figure 4.2. Internal shock structure (TR=1.42)

Mach contours at the inlet's entrance region are visible in Figure 4.3: the computed results agree well with Newsome's solution and with the Schlieren images from Nagashima et al.'s experiment.

The normalised static pressure field inside the inlet is shown in Figure 4.4. Pressure values taken at the locations of the experimental sensors are in accordance with Nagashima's findings (Table 4.1), with the exception of sensor P3. This discrepancy was also observed by Newsome, and might be due to the particular position of the probe, which is located near the internal shock waves system region.

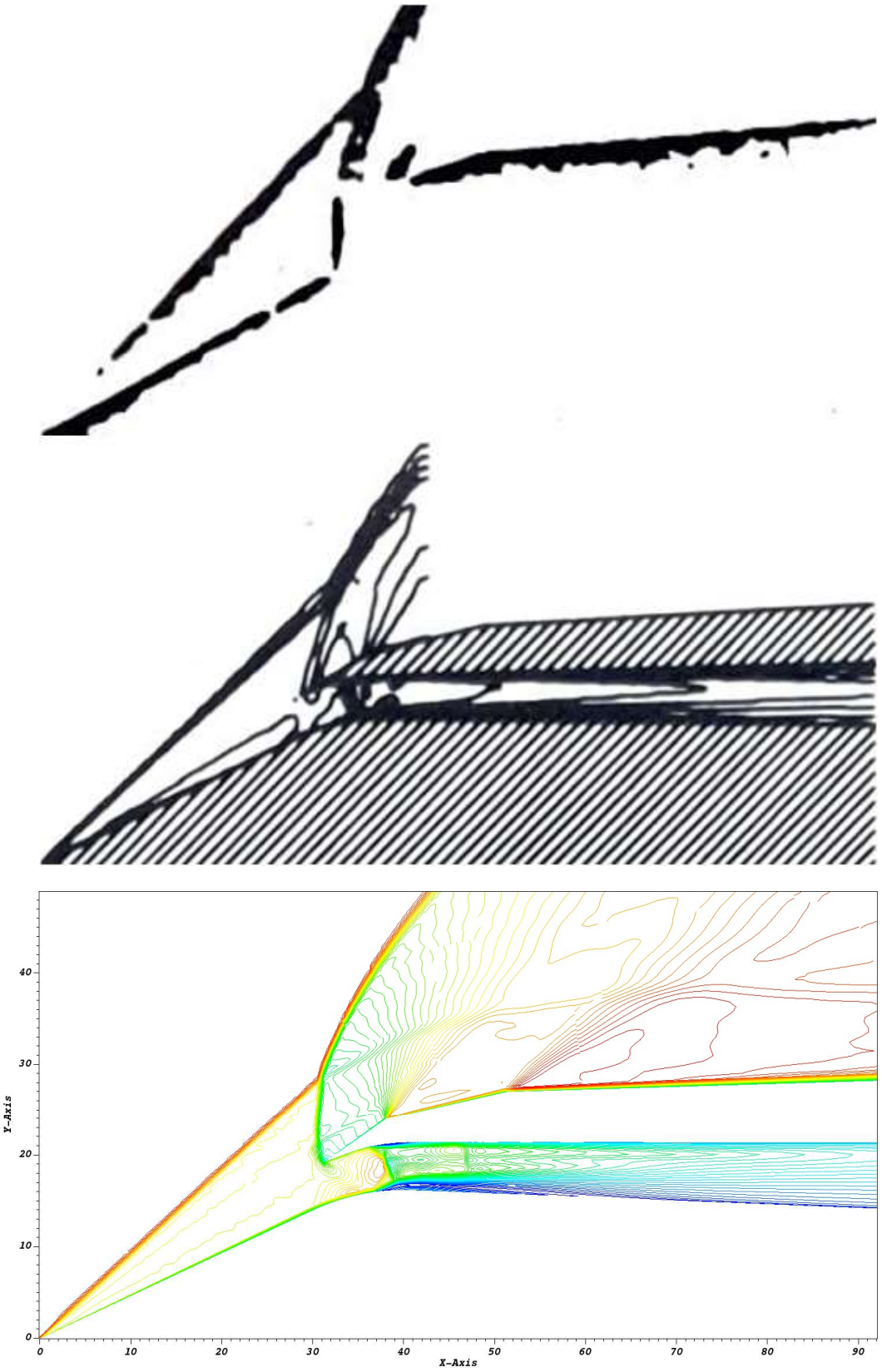

Figure 4.3. Schlieren photograph ([1], top) vs. Mach contours ([12], middle; bottom) (TR=1.42)

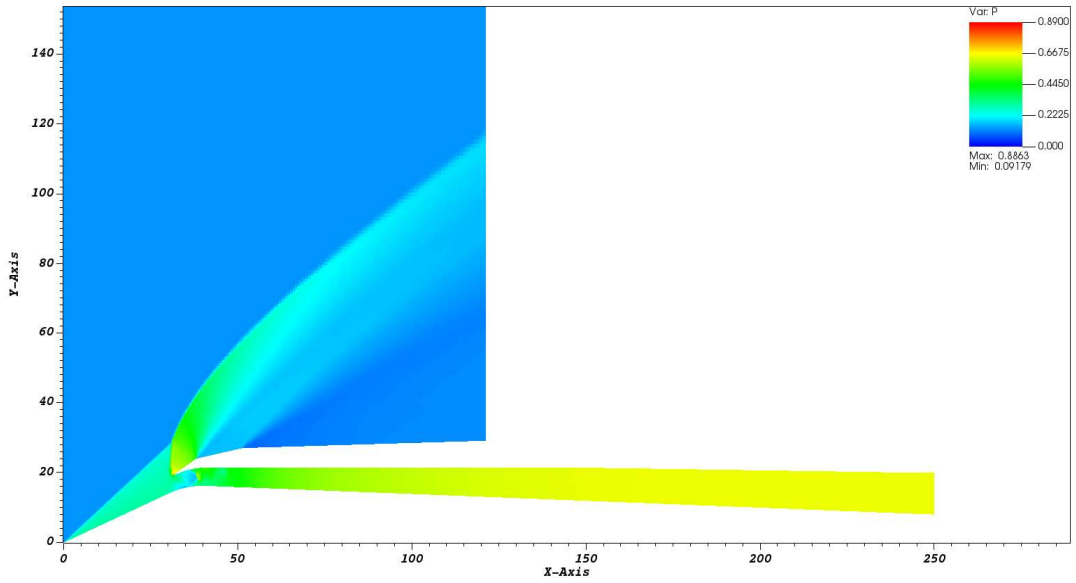

Figure 4.4. Normalised static pressure field (TR=1.42)

Sensor	Experimental value	Computed value
P1	0.30	0.30
P2	0.32	0.30
P3	0.26	0.38
P4	0.65	0.64
P5	0.67	0.65

Table 4.1. Normalised static pressure values at the experimental sensors' locations: comparison between experimental and numerical results (TR=1.42)

4.2. Subcritical case (TR=0.67)

The steady-state solution of the near-critical case has served as the starting point for the simulation of a subcritical operating condition, referred to as *TR=0.67* in Nagashima's paper, which has also been analysed by Hong [16] and Luo et al. [17]. This throttle ratio value corresponds to a normalised mean static pressure $p_n \approx 0.77$ at the subsonic outlet of our domain.

As explained in Section 2.6, changes in engine throttle that cause a decrease in the mass-flow ratio value may lead, under certain circumstances, to the onset of an oscillatory phenomenon known as *buzz*: in this particular case, buzz cycles of the *Dailey type* were experimentally observed.

Figure 4.5 shows the comparison between the computed flow field and the Schlieren images from Nagashima's work, and demonstrates that the *subcritical phase* of the cycle is accurately described by the numerical solution. A shock-induced boundary

layer separation, which progressively obstructs the inlet's entrance, and the terminal shock wave moving towards the ramp's tip can be noticed.

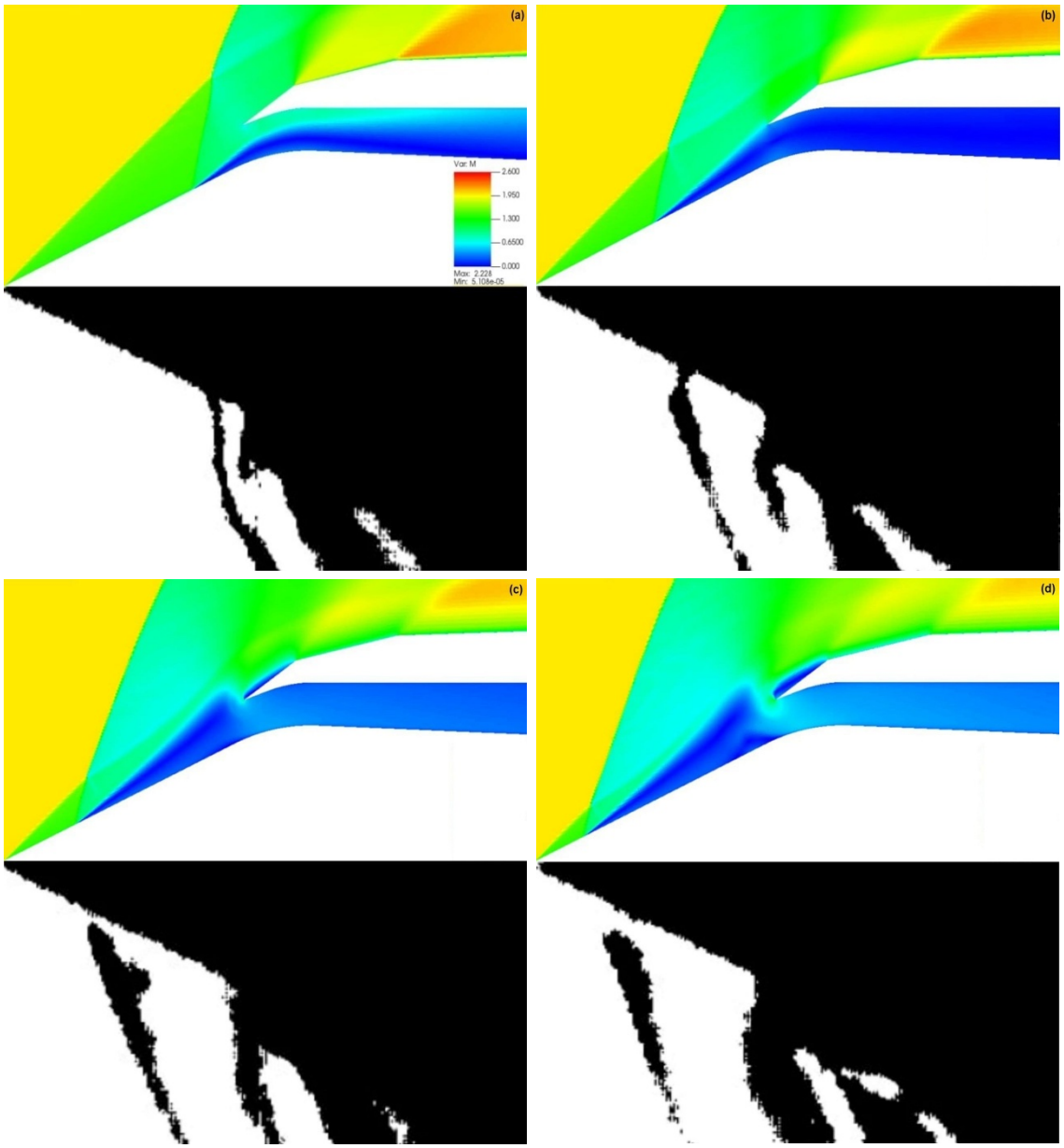

Figure 4.5. Computed Mach number distribution vs. Schlieren photographs [1] - subcritical phase (TR=0.67)

A further comparison between our results and Hong's Mach number distribution for the subcritical phase, presented in Figure 4.6, shows that the two numerical solutions agree well.

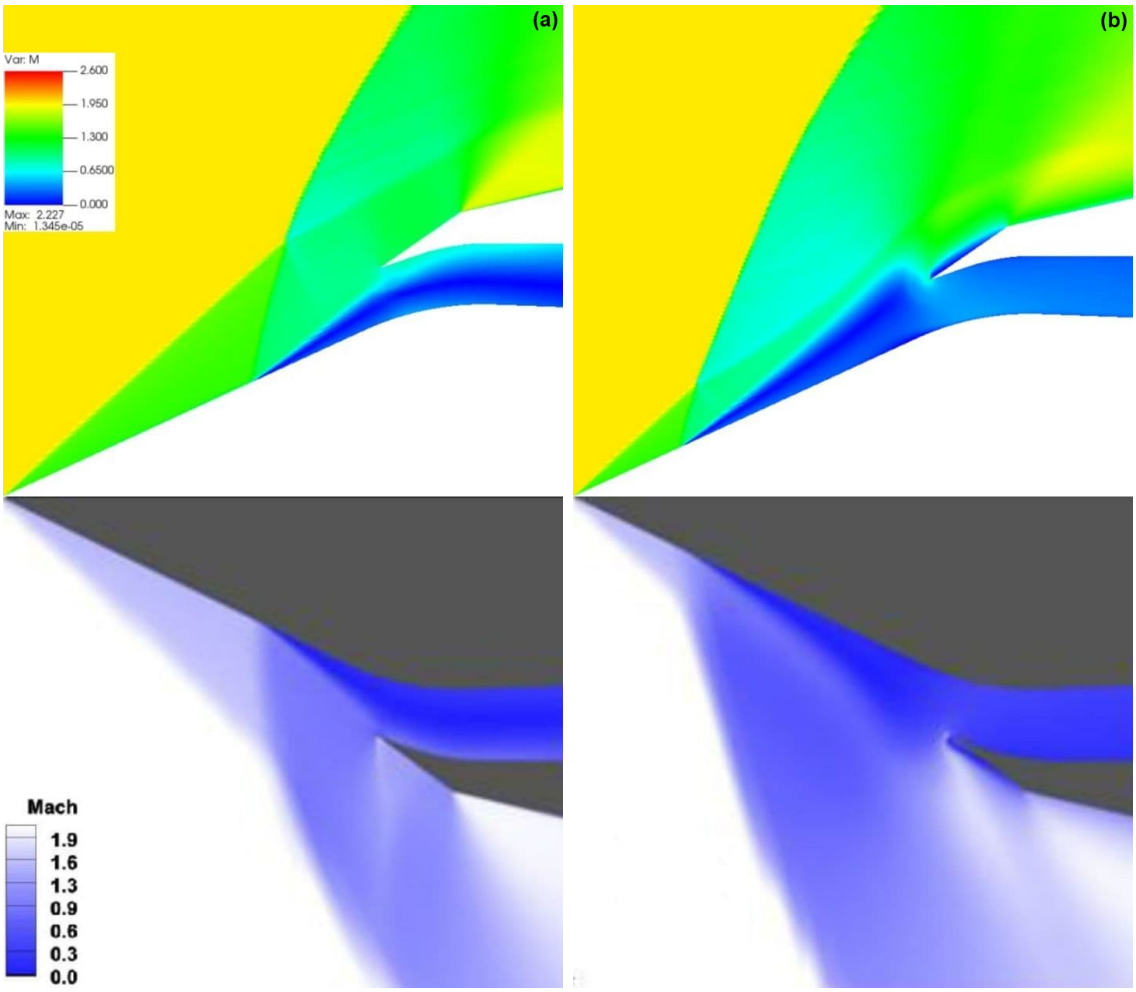

Figure 4.6. Mach number distribution: comparison between two different numerical solutions [16] - subcritical phase (TR=0.67)

However, during the shock's retreat stage, which theoretically precedes the *supercritical phase*, several oscillations of the system are observed in the numerical flow field as the terminal shock wave moves back and forth on the compression ramp (Figure 4.7). This motion, which does not reproduce the experimentally observed behaviour of the fluid, is characterised by an increasing amplitude and is somewhat irregular, as shown by the computed pressure histories in Figure 4.8. The contemporaneous presence of a separated flow area that blocks the inlet's entrance furthermore prevents the shock from reaching its supercritical position: the last part of the buzz cycle is not faithfully replicated.

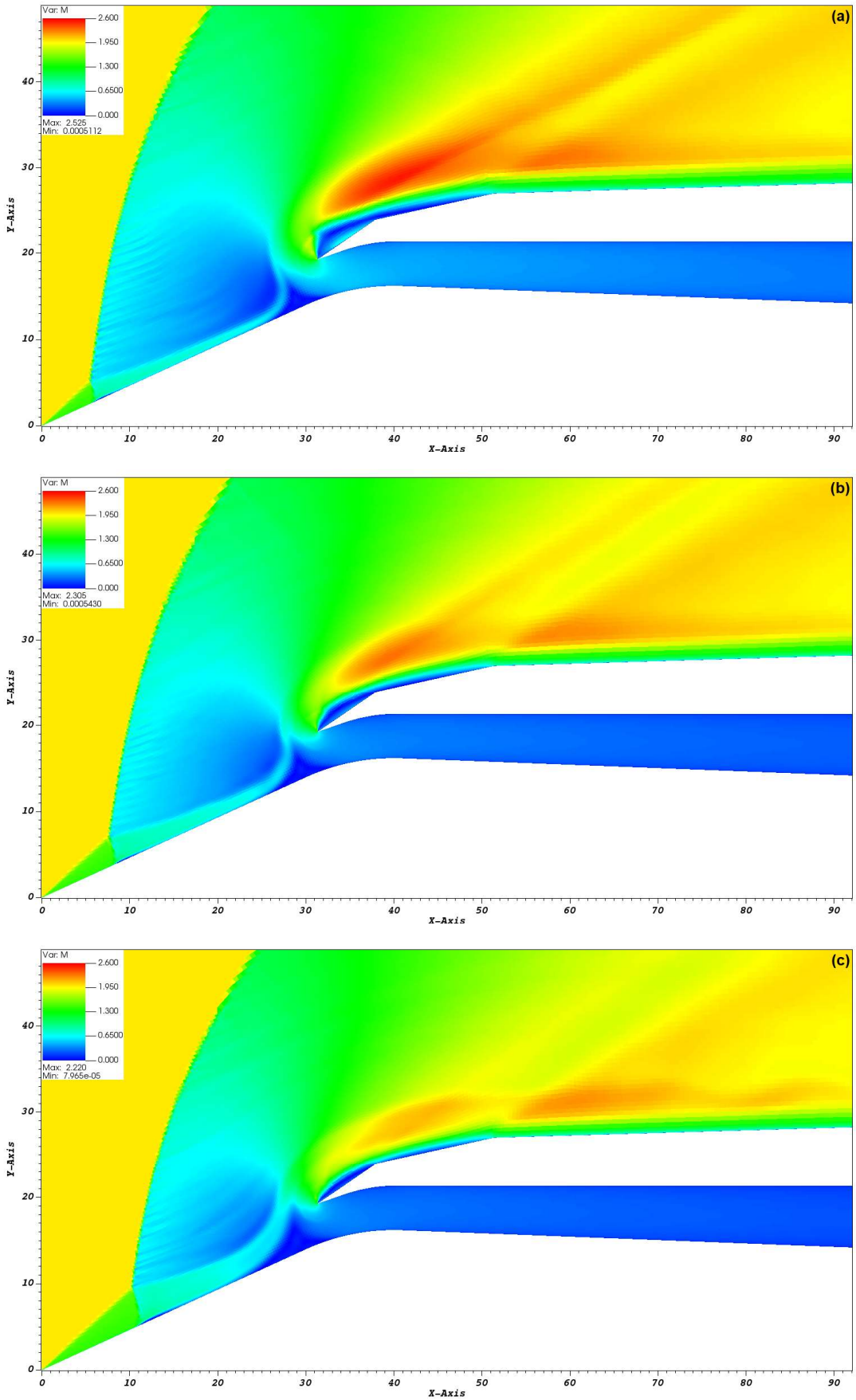

Figure 4.7 (a-c). Shock oscillations during the retreat phase (TR=0.67)

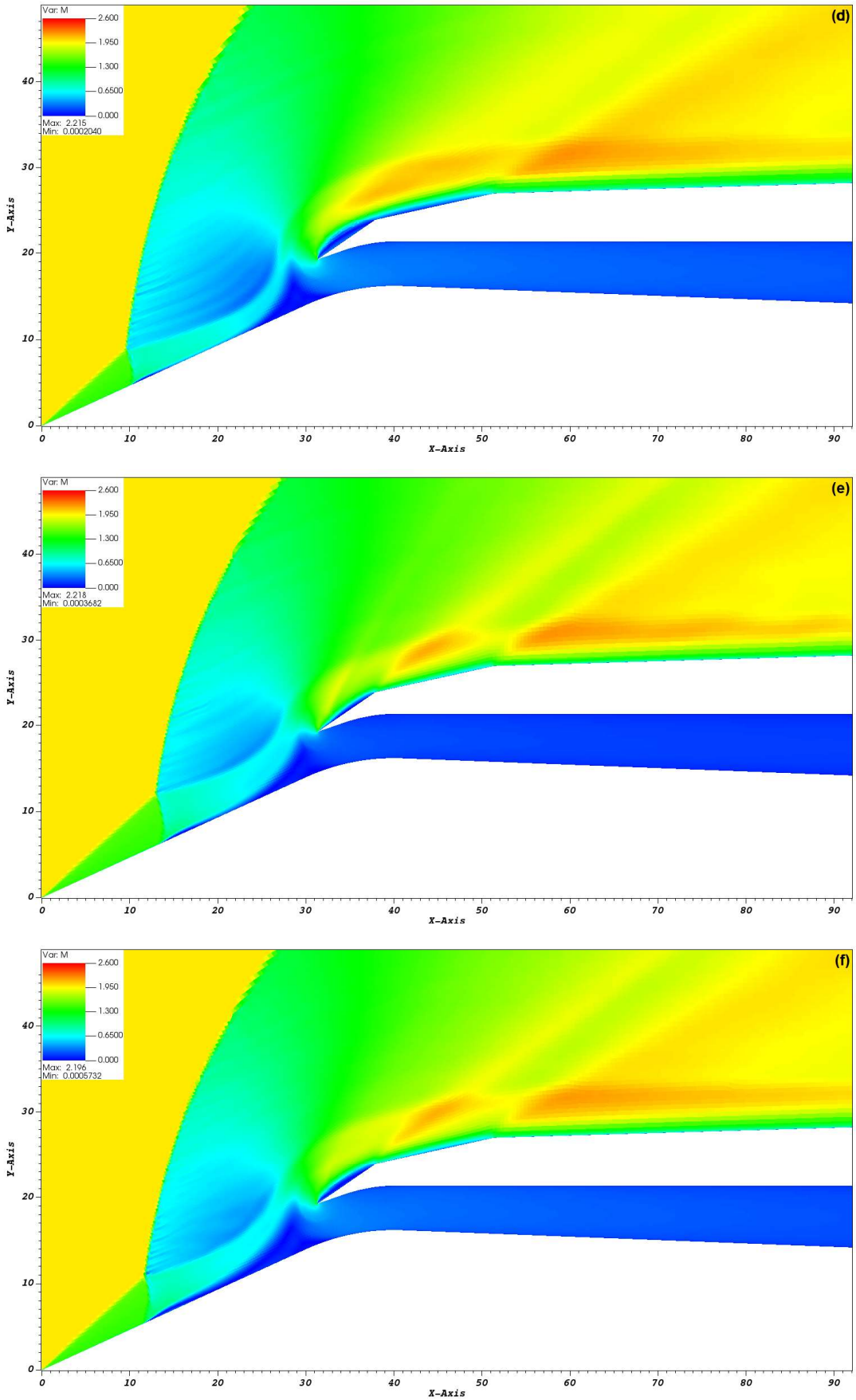

Figure 4.7 (d-f). Shock oscillations during the retreat phase (TR=0.67)

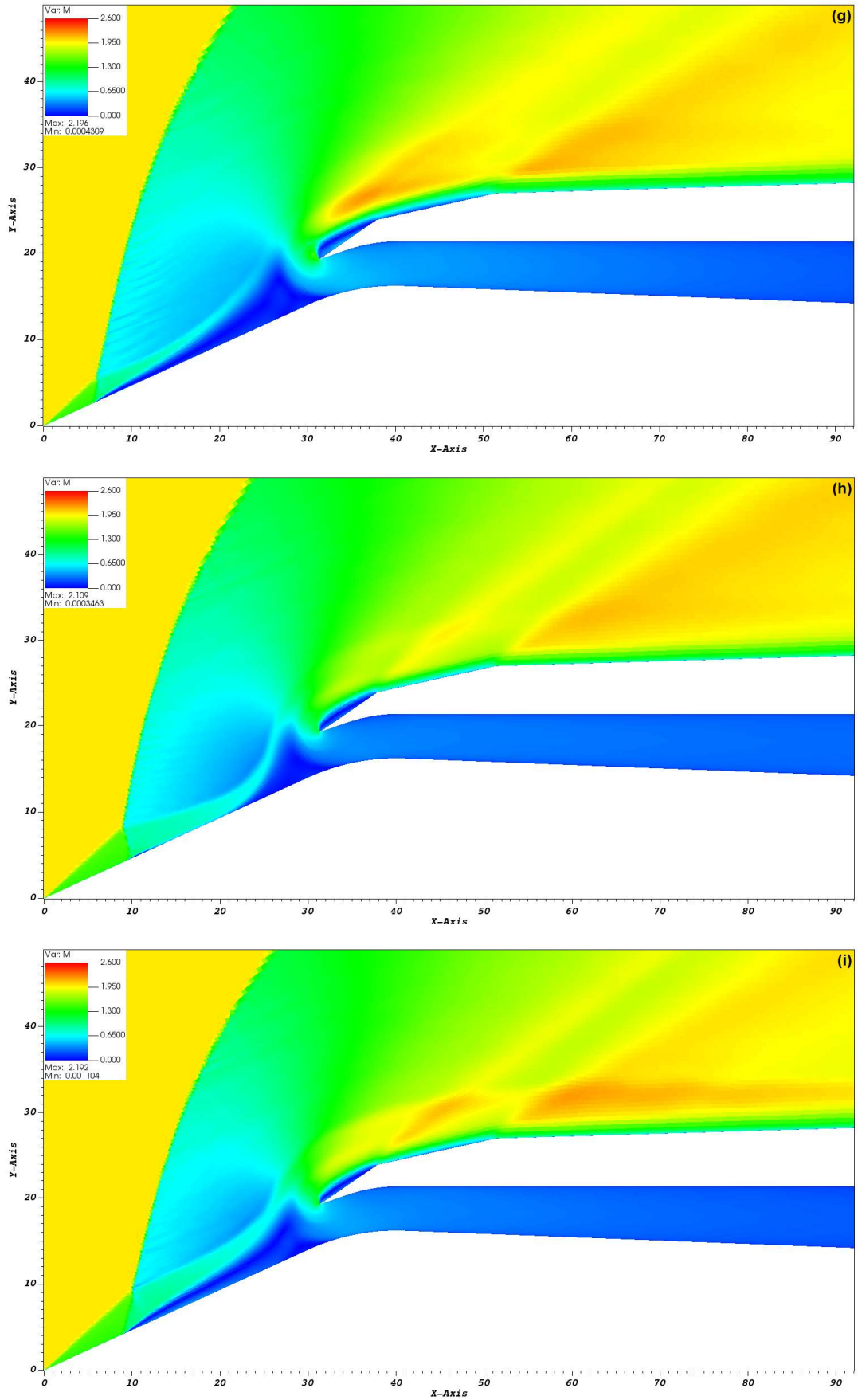

Figure 4.7 (g-i). Shock oscillations during the retreat phase (TR=0.67)

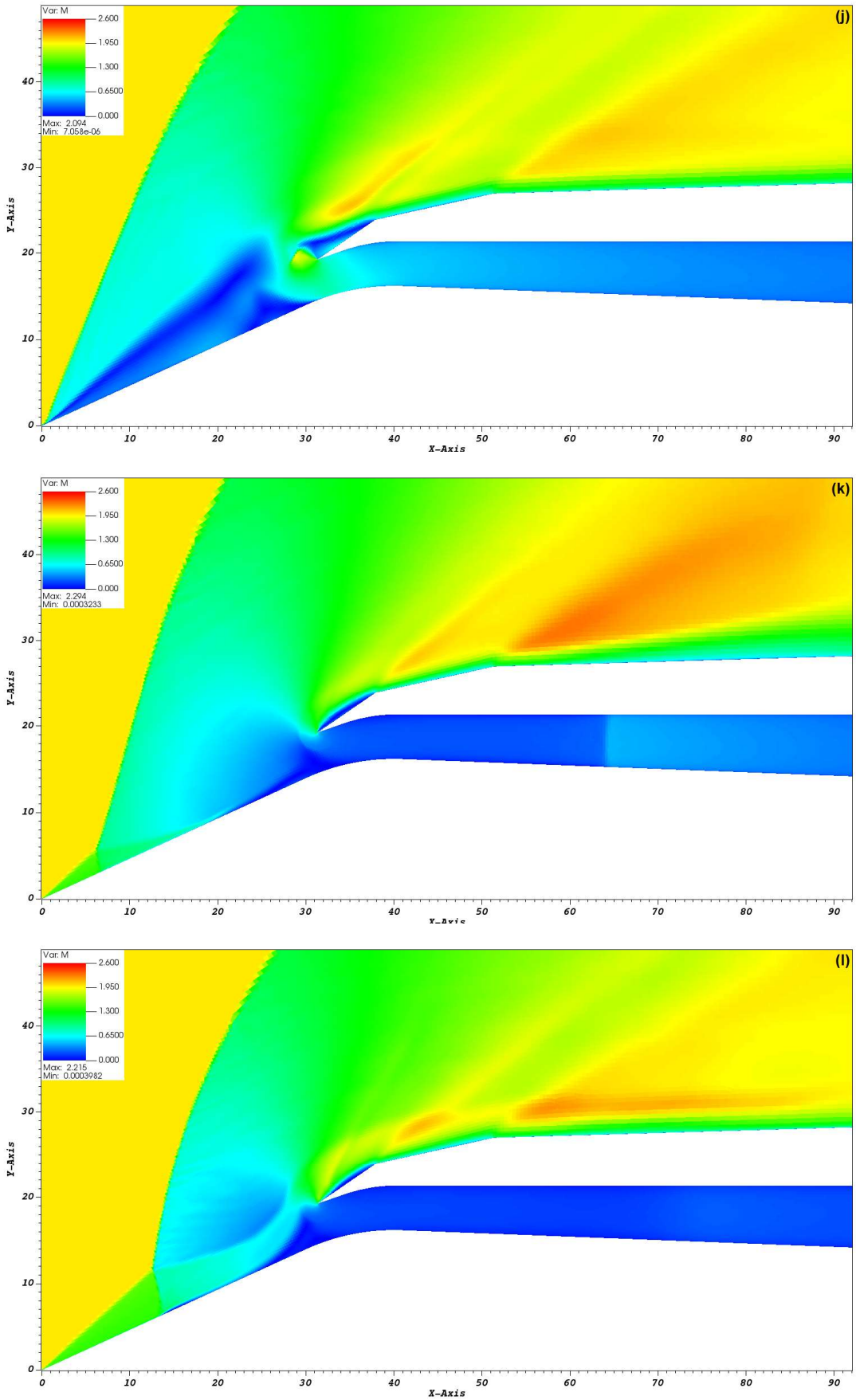

Figure 4.7 (j-l). Shock oscillations during the retreat phase (TR=0.67)

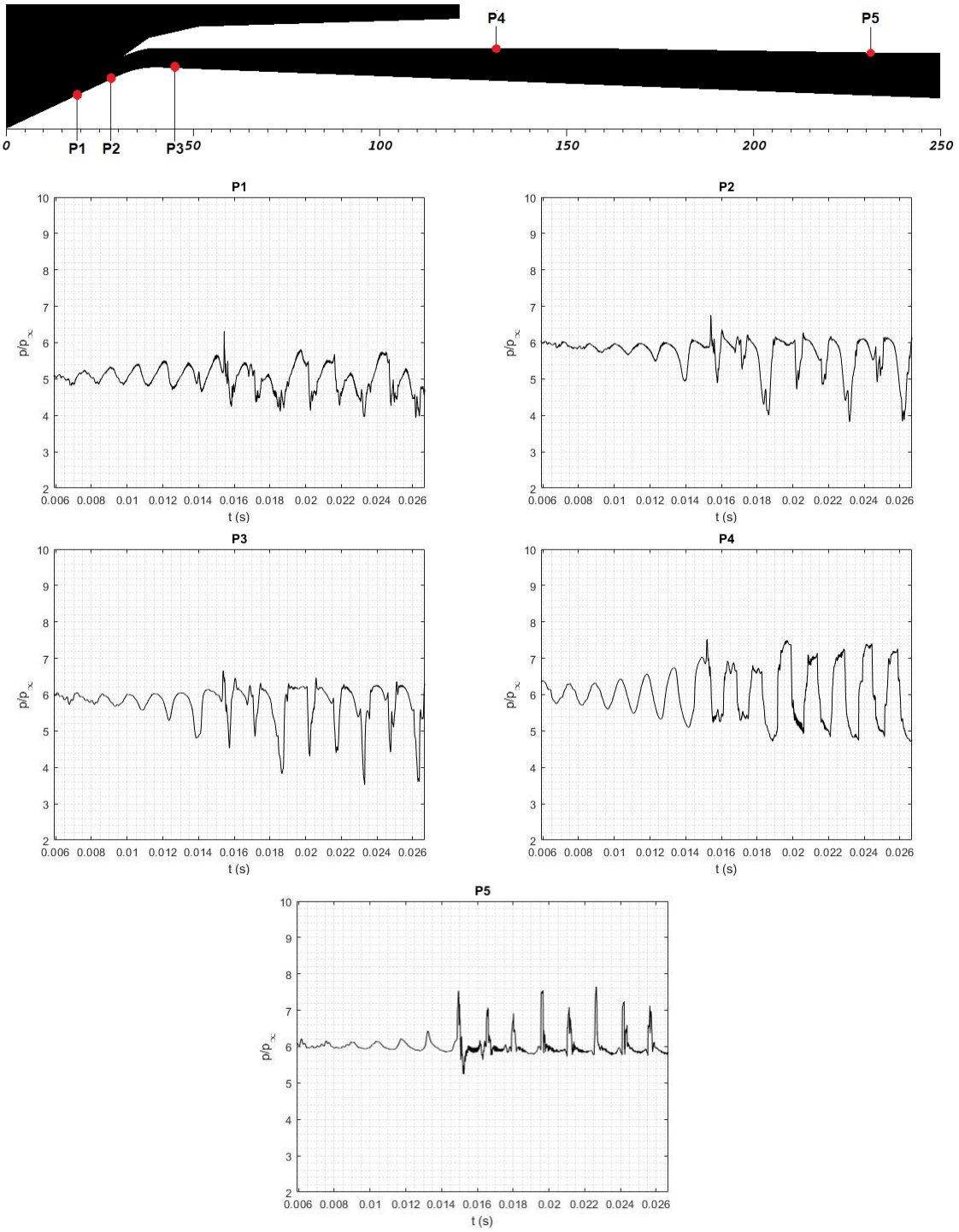

Figure 4.8. Computed pressure histories at the experimental sensors' locations (TR=0.67)

The numerical results for sensors P2 and P3 are also compared with the experimental solution in Figure 4.9, where the non-cyclic pattern of the computed pressure signals is emphasised.

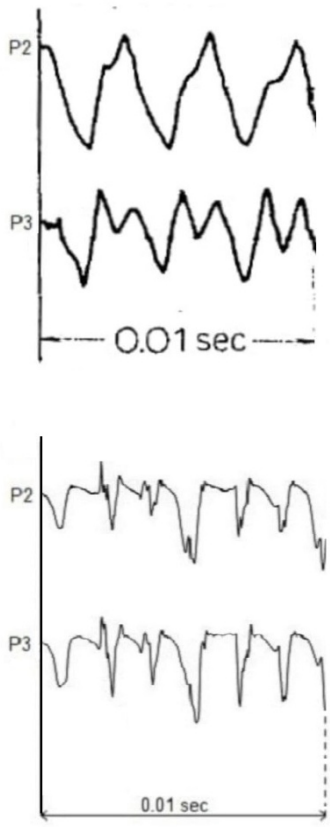

Figure 4.9. Comparison between the experimental ([1], top) and numerical (bottom) pressure histories (TR=0.67)

Despite the solver's capability to capture flow instability under this specific subcritical operating condition, the obtained results appear to be distant from the experimental findings. The behaviour of the numerical solution can be attributed to different causes. Firstly, the relatively coarse mesh (see Section 3.2.1) generated for this preliminary analysis of the buzz phenomenon may have negatively influenced the computed flow field: a grid convergence study should therefore be conducted in order to investigate the effects of further mesh refinements on the solution. Additionally, physics-based explanations can be provided considering an aeroacustics perspective. Due to computational reasons, mainly associated with the limited available time for the running of our simulations, the inlet's length in the present work has been reduced in comparison with Nagashima's experimental model. However, as highlighted in Section 2.6.2, buzz is regarded as a self-excited phenomenon, which can only be sustained if a positive *feedback mechanism* is present: since such mechanism is dependent on the geometrical features of the inlet [10], [13], the computed buzz cycle may have been affected by the length modification. Furthermore, it can be noted that the shortened inlet's exit is located at a position where large static pressure variations throughout a single buzz cycle have been observed in Luo et al.'s analysis [17] (Figure 4.10): the imposed pressure outlet condition has therefore acted as a non-physical constraint,

forcing the local pressure oscillations to be reduced in magnitude. This limiting action can be seen from probe P5's pressure history (Figure 4.8), which highlights that the signal's amplitude is rather small in comparison to the nearest sensor P4.

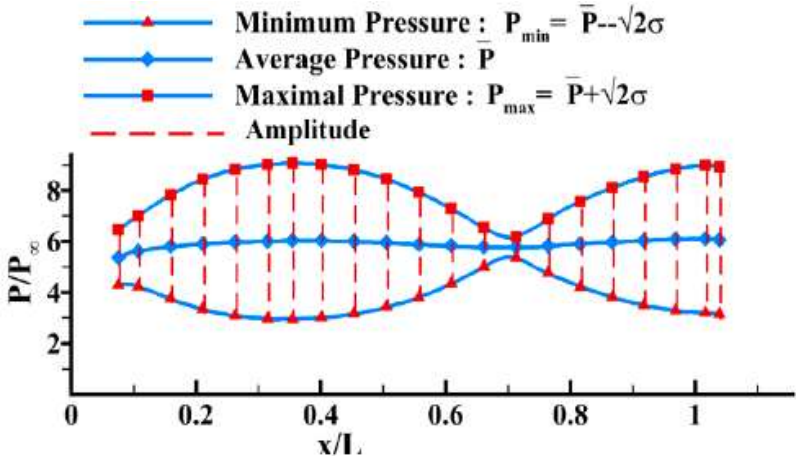

Figure 4.10. Pressure standard deviation distribution inside the inlet [17] (TR=0.67). Here, L=0.635m is the experimental inlet model's length

Lastly, it must be noticed that, starting from the onset of the instability, only a brief period of physical time has been simulated: a much larger number of iterations might be needed in order to observe an evolution of the flow field towards a possible periodical solution. Clearly, additional computational resources are necessary to fulfil such requirement.

5. Conclusions and future perspectives

The flow field in an experimentally tested axisymmetric, external compression supersonic inlet operating at near-critical and subcritical off-design conditions has been investigated numerically.

The simulations have been performed exploiting a research CFD code, based on an unstructured finite volumes method and on the Unsteady-RANS approach combined with the Spalart-Allmaras turbulence model. A second-order accurate upwind scheme has been used for the spatial discretisation of the governing equations, and the Barth and Jespersen limiter has been implemented in order to avoid spurious oscillations in the computed solution. Moreover, depending on the simulated regime, different implicit temporal discretisation schemes and Courant numbers have been chosen.

The solver has been successfully validated for the near-critical, steady-state condition: the obtained results are in good agreement with the experimental findings, as well as with a previous numerical analysis performed on the same case. Nevertheless, the unstable subcritical regime, for which buzz cycles of the *Dailey type* were experimentally observed, has not been correctly reproduced: notwithstanding the solver's capability to capture flow instability under this specific operating condition, the computed solution appears to be distant from the experimental results. Explanations for the behaviour of the numerical flow field can be provided considering different perspectives: on the one hand, the relatively coarse mesh generated for this preliminary analysis of buzz may have negatively influenced the solution; on the other hand, buzz characteristics might have been affected by the reduced length of the computational inlet model and by the imposed constant static pressure at the inlet's exit, which acts as a constraint on the local pressure variations.

In view of the above, a grid convergence analysis should be conducted in order to carefully investigate the impact of further mesh refinements on the computed results; different lengths of the inlet should also be considered, so as to locate its exit in a position where pressure oscillations during buzz are a minimum: a deeper knowledge of the phenomenon from an analytical point of view is therefore desirable. Lastly, a much larger number of iterations might be needed in order to observe an evolution of the flow field towards a possible periodical solution. Undoubtedly, additional computational resources, in terms of both time and power, are necessary for the accomplishment of these tasks.

Acknowledgements

The author would like to acknowledge his gratitude to professors Francesco Larocca and Andrea Ferrero for their invaluable guidance throughout these months of intense work.
Thanks are also due to HPC@POLITO, a project of Academic Computing within the Department of Control and Computer Engineering at the Politecnico di Torino, which provided the computational resources necessary for the running of the numerical simulations.
The author furthermore wishes to thank his family and friends for their continued and unconditional support. In order to do so, a separate acknowledgments section has been written in Italian.

Acknowledgements (Italian version)

I più sentiti ringraziamenti vanno innanzitutto alla mia famiglia, che ha sempre saputo essere presente e supportarmi, durante i miei anni da studente, attraverso l'affetto, la disponibilità ad assecondare le mie esigenze e la comprensione durante i momenti di difficoltà, oltre che attraverso preziosi consigli ed aiuti.
È inoltre doveroso da parte mia ringraziare, seppur sinteticamente, gli amici che ho avuto la fortuna di incontrare nel mio percorso, ed il cui contributo si è dimostrato fondamentale per la mia crescita, sia accademica che personale. Grazie dunque a Michele, per essere stato al mio fianco da quando ho memoria, ed a Francesco, Ciro, Carmine, Lorenzo, Gaia e Remigio, che formano il miglior gruppo di amici di lunga data che potessi desiderare. Grazie a Toti, Giovannino, Carlo, Giorgio, Alessia, Andrea S., Oronzo, Andrea C., Sofia, Antonio, Davide, Federica, Paola e Gianluca, con i quali numerose conoscenze ed esperienze sono state condivise sia all'interno che al di fuori del Politecnico. Grazie a Giacomo, Gennaro, Bruno, Simone, Daniele, Felice, Benedetta e Maria, per avermi mostrato l'importanza di migliorarsi costantemente. Grazie a Marica, per i suoi incoraggiamenti e la sua capacità di trasmettermi ottimismo. Grazie ai ragazzi ed alle ragazze della *Elio United*, della *Calcio e Beppe* e del *Polito Sailing Team*, troppo numerosi per essere citati individualmente, dimostratisi buoni amici oltre che eccellenti compagni di squadra.
Un ringraziamento particolare, infine, va a Cristina, coinquilina, amica e compagna straordinaria, per il suo incondizionato amore e sostegno nei miei confronti.
Il supporto di queste persone nel tempo si è rivelato per me di primaria importanza, ed è per tale motivo che il presente lavoro è, in parte, dedicato anche a loro.

Bibliography

[1] T. Nagashima, T. Obokata, and A. Tsuyoshi, “Experiment of Supersonic Air Intake Buzz,” Institute of Space and Aeronautical Science, University of Tokyo, 1972.

[2] J. Seddon and E. L. Goldsmith, *Intake Aerodynamics*, 2nd ed. AIAA Education Series, AIAA, 1999.

[3] J. D. Mattingly, W. H. Heiser, and D. T. Pratt, *Aircraft Engine Design*, 2nd ed. AIAA Education Series, AIAA, 2002.

[4] M. Kaushik, “Compressible Flows,” in *Theoretical and Experimental Aerodynamics*, Springer, Singapore, 2019.

[5] Y. Gordon and B. Gunston, *Soviet X-Planes*. Midland Publishing, 2000.

[6] K. Oswatitsch, “Pressure Recovery for Missiles with Reaction Propulsion at High Supersonic Speeds (The Efficiency of Shock Diffusers),” NACA TM No. 1140, 1947.

[7] A. Ferri and L. M. Nucci, “The Origin of Aerodynamic Instability of Supersonic Inlets at Subcritical Conditions,” NACA RM L50K30, 1951.

[8] C. L. Dailey, “Supersonic Diffuser Instability,” California Institute of Technology, 1954.

[9] R. V. Chima, “Analysis of Buzz in a Supersonic Inlet,” *NASA Tech. Memo.*, no. NASA/TM--2012-217612, 2012.

[10] W. L. Hankey and J. S. Shang, “Analysis of Self-Excited Oscillations in Fluid Flows,” AIAA Paper 80-1346, 1980.

[11] J. E. Rossiter, “Wind tunnel experiments on the flow over rectangular cavities at subsonic and transonic speeds,” R&M No. 3438, British ARC, 1964.

[12] R. W. Newsome, “Numerical Simulation of Near-Critical and Unsteady, Subcritical Inlet Flow,” *AIAA J.*, vol. 22, no. 10, pp. 1375–1379, 1984.

[13] P.-J. Lu and L.-T. Jain, “On the Numerical Investigation of Inlet Buzz Flow,” in *20th Congress of the International Council of the Aeronautical Science*, 1996.

[14] S. Trapier, P. Duveau, and S. Deck, “Experimental Study of Supersonic Inlet Buzz,” *AIAA J.*, vol. 44, no. 10, 2006.

[15] S. Trapier, P. Duveau, and S. Deck, “Delayed Detached-Eddy Simulation and Analysis of Supersonic Inlet Buzz,” *AIAA J.*, vol. 46, no. 1, 2008.

[16] W. Hong, “Numerical Analysis of Supersonic Inlet Buzz Characteristics under Various Throttling and Angle of Attack Conditions,” Seoul National University, 2013.

[17] W. Luo, Y. Wei, K. Dai, J. Zhu, and Y. You, “Spatiotemporal Characterization and Suppression Mechanism of Supersonic Inlet Buzz with Proper Orthogonal Decomposition Method,” *Energies*, vol. 13, no. 217, 2020.

[18] J. L. Lumley, “The Structure of Inhomogeneous Turbulent Flows,” in *Atmospheric Turbulence and Radio Wave Propagation*, A. M. Yaglom and V. I.

Tartarsky, Eds. 1967, pp. 166–177.

[19] J. Blazek, *Computational Fluid Dynamics: Principles and Applications*, 3rd ed. Elsevier, 2015.

[20] H. K. Versteeg and W. Malalasekera, *An Introduction to Computational Fluid Dynamics - The Finite Volume Method*, 2nd ed. Pearson Education Limited, 2007.

[21] C. Geuzaine and J.-F. Remacle, “Gmsh: a three-dimensional finite element mesh generator with built-in pre- and post-processing facilities,” *Int. J. Numer. Methods Eng.*, vol. 79, no. 11, pp. 1309–1331, 2009.

[22] J.-F. Remacle *et al.*, “A frontal Delaunay quad mesh generator using the Linf norm,” *Int. J. Numer. Methods Eng.*, vol. 94, no. 5, pp. 494–512, 2013.

[23] J.-F. Remacle, J. Lambrechts, B. Seny, E. Marchandise, A. Johnen, and C. Geuzaine, “Blossom-Quad: a non-uniform quadrilateral mesh generator using a minimum cost perfect matching algorithm,” *Int. J. Numer. Methods Eng.*, vol. 89, pp. 1102–1119, 2012.

[24] T. J. Barth and D. C. Jespersen, “The Design and Application of Upwind Schemes on Unstructured Meshes,” *AIAA Pap.*, vol. 89, no. 366, 1989.

[25] C. F. Ollivier-Grooch, “Towards Problem-Independent Multigrid Convergence Rates for Unstructured Mesh Methods,” in *6th Int. Symp. CFD*, 1995.

[26] A. Jameson, “Solution of the Euler Equations by a Multigrid Method,” *Appl. Math. Comput.*, vol. 13, 1983.

[27] A. Brandt, “Guide to multigrid development,” in *Hackbush W., Trottenberg U. (eds) Multigrid Methods. Lecture Notes in Mathematics, Vol. 960*, Springer, Berlin, Heidelberg, 1981.

[28] R. Courant, K. O. Friedrichs, and H. Lewy, “On the Partial Difference Equations of Mathematical Physics,” *IBM J.*, vol. 11, 1967.

[29] D. A. Anderson, J. C. Tannehill, and R. H. Pletcher, *Computational Fluid Mechanics and Heat Transfer*. Hemisphere, 1984.

[30] J. Boussinesq, “Essai sur la théorie des eaux courantes.” Mem. Pres. Acad. Sci, XXIII, 46, 1877.

[31] P. R. Spalart and S. R. Allmaras, “A One-Equation Turbulence Model For Aerodynamic Flows,” in *AIAA 30th Aerospace Sciences Meeting and Exhibit*, 1992.

[32] “VisIt.” Department of Energy (DOE) Advanced Simulation and Computing Initiative (ASCI), Lawrence Livermore National Laboratory, 2002.